





RESEARCH ARTICLE | APRIL 25 2023

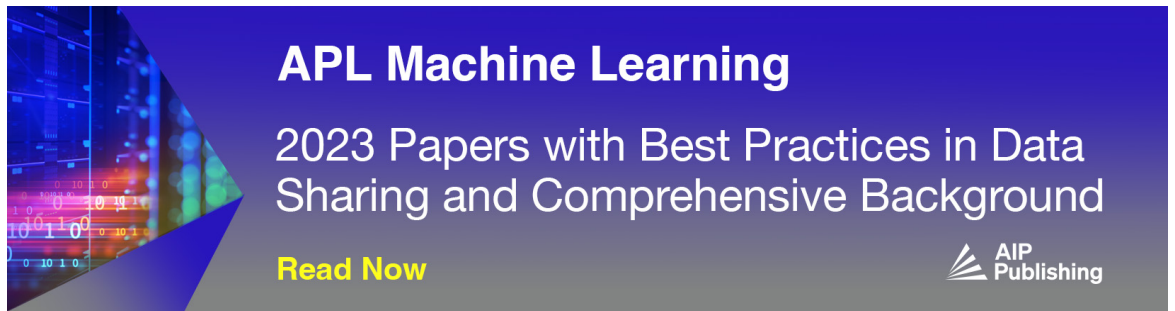
The optimization of the compact upwind scheme for incompressible flow

Ding Hao (丁昊) ; Chen Yu-Jie (陈宇杰) ; Tao Wen-Quan (陶文铨)  



Physics of Fluids 35, 045148 (2023)


<https://doi.org/10.1063/5.0146773>



APL Machine Learning

2023 Papers with Best Practices in Data Sharing and Comprehensive Background

[Read Now](#)



The optimization of the compact upwind scheme for incompressible flow

Cite as: Phys. Fluids **35**, 045148 (2023); doi: [10.1063/5.0146773](https://doi.org/10.1063/5.0146773)

Submitted: 16 February 2023 · Accepted: 6 April 2023 ·

Published Online: 25 April 2023





View Online



Export Citation



CrossMark

Hao Ding (丁昊), , Yu-Jie Chen (陈宇杰), , and Wen-Quan Tao (陶文铨)^{a)} 

AFFILIATIONS

Key Laboratory of Thermo-Fluid Science and Engineering, Ministry of Education, School of Energy & Power Engineering, Xi'an Jiaotong University, Shaanxi 710049, China

^{a)} Author to whom correspondence should be addressed: wqtao@mail.xjtu.edu.cn

ABSTRACT

Different compact upwind schemes have been developed and used to numerically approximate a convection term in the Navier–Stokes equation. With different point stencils, the compact upwind schemes are mainly classified as the central, the function-biased, and the derivative-biased compact upwind schemes. They have different numerical characteristics. In this paper, by using Fourier analysis and numerical test, it is found that the function-biased compact upwind schemes have better resolution properties than the derivative-biased compact upwind schemes. Furthermore, an optimization method named dispersion-dissipation-balancing (DDB) optimization is proposed, by which better spectral resolution of these schemes is obtained by optimizing coefficients of these schemes based on the balance between a dispersion error and a dissipation error. Compared with the popular dispersion-relation-preserving (DRP) optimization method, the schemes optimized by the DDB method have proper dispersion and dissipation errors. They eliminate both the nonphysical oscillations and spurious vortices in the numerical case of the double shear layers flow. In addition, the central compact upwind scheme optimized by the DDB method (OCCUS_DDB) has the best performance among the schemes studied in this paper.

Published under an exclusive license by AIP Publishing. <https://doi.org/10.1063/5.0146773>

I. INTRODUCTION

Fluid flow characteristics can be described by the Navier–Stokes (N-S) equation, which is usually discretized and solved by numerical methods. The discretization scheme of the nonlinear convection term of the N-S equation significantly affects the accuracy and stability of the numerical solution. Many discretization schemes of the convection term have been proposed and widely used in different problems. The high-order compact scheme can achieve high accuracy and high resolution with few stencil points. It has attracted extensive attention since Lele¹ proposed the symmetric compact schemes and systematically analyzed their resolution characteristics. It is to be noted here that the term functioning the effect of fluid flow in the N-S equation is usually termed as convection. When the N-S equation is reduced to an equation without the diffusion term, this term is called advection. In this paper, we adopt the conventional practice and call it convection throughout the paper.

The traditional difference scheme for the convection term, a kind of spatial-explicit scheme, uses the combination of function values at different locations to approximate the targeted first-order derivative value. Differently, what the compact scheme approximates is the combination of the first derivative values. The expression of a single

derivative cannot be given explicitly by function values, so the compact schemes are spatial-implicit schemes. Compared with the spatial-explicit finite difference schemes, the compact schemes can achieve the same order of accuracy with a narrower stencil, reducing the workload of boundary discretization. In addition, when writing the compact schemes in a matrix form, it can be found that the compact schemes use much more points to approximate the derivative than the spatial-explicit schemes,^{2–4} so the compact schemes have a higher spectral resolution. For these reasons, the compact schemes are widely used in the numerical discretization of the N-S equation for solving the flows with multi-scale structures, such as the direct and large eddy simulation of turbulence flow or aeroacoustics process.^{5–10}

When applying the symmetric compact central schemes to discretize the nonlinear convection term, the high wavenumber components beyond the upper resolved limit will be wrongly regarded as the low wavenumber components. This kind of error is termed aliasing error, which will lead to spectral blocking, the accumulation of noise at high wavenumbers. Due to the aliasing error, nonphysical oscillation will occur and finally causes numerical instability. The compact upwind schemes with inherent dissipation at the high wavenumber region can dissipate the spectral blocking and depress the aliasing

error.¹¹ Therefore, the upwind scheme is preferable in the direct numerical simulation of strong flow problems. The compact upwind schemes can be expressed in the following general form:

$$\sum_{k=-r}^s a_k u'_{i+k} = \sum_{l=-p}^q b_l u_{i+l}, \tag{1}$$

where a_k are the coefficients of the first-order derivatives; b_l are the coefficients of functions; $p, q, r,$ and s are the positive integers, which decide the stencil of discrete points. In this paper, the compact upwind scheme is divided into four categories according to the point stencil used: the central compact upwind scheme ($r = s, p = q$), derivative-biased compact upwind scheme ($r > s, p = q$), function-biased compact upwind scheme ($r = s, p > q$), and all-biased compact upwind scheme ($r > s, p > q$). Our study will be focused on the cases with $u > 0$, and extension to the cases of $u < 0$ will be briefly mentioned in the later discussion.

The central compact upwind scheme (CCUS) uses the same stencil as the symmetric compact central scheme, but its coefficients are asymmetric. It can be constructed by adding extra dissipation to the symmetric compact central scheme.^{2,12,13} For the compact upwind schemes with the biased stencil, Fu and Ma¹⁴ proposed the derivative-biased compact upwind scheme (DCUS), which has been further developed in Refs. 15 and 16 and has been widely used in many areas.^{16–20} The function-biased compact upwind scheme (FCUS) has the same number of stencil points as DCUS, and its feature of the biased function points is closer to the spatial-explicit upwind scheme in form. To the best of the authors' knowledge, it was not until Fan²¹ proposed the scheme named standard compact upwind scheme in 2016 that FCUS started being adopted in the numerical simulation of incompressible flow problems.^{22–24} Therefore, one of the purposes of this study is to compare the characteristics of these two types of biased schemes. As for the all-biased stencil compact upwind scheme (ACUS), the number of points used in this kind of scheme is the same as the spatial-explicit central scheme with the same order; hence, the scheme practically loses the advantage of compactness. Thus, we will not go into the details of the ACUS in the following presentation.

The compact upwind schemes mentioned above all have a higher resolution than the spatial-explicit upwind schemes. The resolution of a scheme represents the capability to resolve the flow details in different physical scales, which is more important than the order of a scheme in the numerical simulation of flow with multi-scale structures. Usually, higher order schemes have a higher accuracy. However, it is to be noted that the high-order scheme does not always have high spectral resolution.^{1,25} Therefore, the compact scheme is often optimized for high resolution by sacrificing the order. Lele¹ proposed the compact scheme of the fourth-order formal accuracy with a spectral-like resolution, whose resolution characteristics are better than the tenth-order scheme using the same stencil. Li²⁶ constructed a series of wavenumber-extended upwind-biased schemes with high resolution for which the order is lower than that of the spatial-explicit upwind schemes. De and Eswaran²⁷ presented a high-resolution fifth-order compact upwind scheme with five points for derivatives and 13 points for functions. The order of these schemes is not very high, but they all reach a resolution comparable to the spectral method. Numerous studies^{1,15,27–32} were conducted to optimize the resolution properties of compact schemes, among which the most commonly used method is the dispersion-relation-preserving (DRP) optimization proposed by

Tam and Webb²⁹ and improved by Kim and Lee.³³ Various DRP schemes have been widely adopted in numerical simulations.^{8,15,34–38} It is well known that the main errors in the discretization of the first-order derivative are the dissipation error and dispersion error. The dissipation error affects the amplitude of the solved wave, and the dispersion error affects the propagation velocity of the wave. The numerical solution of the predicted wave with excessive dispersion errors cannot propagate at the correct speed, which will also bring nonphysical oscillations. The DRP scheme is designed to preserve the dispersion relation over a considerable range of wavenumbers so that it can keep the resolved components propagating at the correct physical speeds.²⁸ In the study of Tam and Webb,²⁹ the authors proposed a strategy for dispersion and dissipation errors balance, in which the integration of the dispersion and dissipation errors are combined as the objective function by a weight coefficient. However, it is difficult to determine the proper weight coefficient and integration limit in advance for different stencils. Moreover, in the subsequent research, such as Refs. 30, 32, and 38, the object function is often only related to the dispersion error, and the dissipation error is hardly considered while performing the DRP optimization. Whether this treatment of DRP will affect the amplitude of the numerical results remains to be revealed.

As mentioned above, the compact upwind scheme possesses the characteristics of high dissipation at the high wavenumber region, which can decay the high-frequency nonphysical oscillations caused by aliasing and dispersion errors. In this paper, three types of compact upwind schemes are constructed, and the resolution characteristics of the typical schemes are compared. In order to make a proper balance between dissipation and dispersion errors, an optimization method is proposed for optimizing the coefficients of these three types of schemes. Also, comparisons are made with the DRP optimization method by a spectral analysis, and a problem of the propagation of a one-dimensional ramp signal is tested. Finally, the performance of six optimized schemes and three typical schemes is tested by two classical incompressible flow problems.

II. THREE TYPES OF COMPACT UPWIND SCHEMES AND SPATIAL RESOLUTION

In this section, the general difference expression of three types of compact upwind schemes including CCUS, DCUS, and FCUS is constructed. The spatial resolution of the typical schemes for these three types of schemes is compared. Finally, the DRP optimization method is applied to these schemes.

A. Construction of several compact upwind schemes

For convenience of explanation, the compact scheme with a (3, 5) stencil (three points for derivatives and five points for functions at most) is described here, and its unified form is

$$\begin{aligned} & a_{j-1}u'_{j-1} + u'_j + a_{j+1}u'_{j+1} \\ &= \frac{1}{h} (b_{j-2}u_{j-2} + b_{j-1}u_{j-1} + b_j u_j + b_{j+1}u_{j+1} + b_{j+2}u_{j+2}) \\ &+ m \frac{h^4}{5!} u_j^{(5)} + n \frac{h^5}{6!} u_j^{(6)}, \end{aligned} \tag{2}$$

where h represents the uniform mesh size and n and m are the coefficients of truncation error. From Eq. (2), it is obvious that this form of scheme can reach sixth order at most.

The coefficients for the compact upwind scheme depend on the direction of local velocity. In this paper, we only discuss the condition for $u_j > 0$. For $u_j < 0$, just turn the coefficients on the function side into opposite signed numbers and then exchange the order of the coefficients of the upstream and downstream points on both the derivative side and function side, respectively, as shown in the following:

$$a_{j-1}u'_{j-1} + u'_j + a_{j+1}u'_{j+1} = \frac{1}{h}(b_{j-2}u_{j-2} + b_{j-1}u_{j-1} + b_ju_j + b_{j+1}u_{j+1} + b_{j+2}u_{j+2}) \quad u_j > 0, \tag{3}$$

$$a_{j+1}u'_{j-1} + u'_j + a_{j-1}u'_{j+1} = -\frac{1}{h}(b_{j+2}u_{j-2} + b_{j+1}u_{j-1} + b_ju_j + b_{j-1}u_{j+1} + b_{j-2}u_{j+2}) \quad u_j < 0. \tag{4}$$

In the following, the way of how to derive the three types of compact upwind schemes is introduced in detail.

If $m = 0$, and the coefficients of the functions and derivatives in Eq. (2) are all non-zero, then the scheme is the CCUS with at least fifth-order accuracy. Seven equations with undetermined coefficients are obtained by using the Taylor series expansion, and they are

$$\begin{cases} 0 = b_{j-2} + b_{j-1} + b_j + b_{j+1} + b_{j+2} \\ a_{j-1} + 1 + a_{j+1} = -2b_{j-2} - b_{j-1} + b_{j+1} + 2b_{j+2} \\ -a_{j-1} + a_{j+1} = \frac{1}{2!}(4b_{j-2} + b_{j-1} + b_{j+1} + 4b_{j+2}) \\ \frac{1}{2!}(a_{j-1} + a_{j+1}) = \frac{1}{3!}(-8b_{j-2} - b_{j-1} + b_{j+1} + 8b_{j+2}) \\ \frac{1}{3!}(-a_{j-1} + a_{j+1}) = \frac{1}{4!}(16b_{j-2} + b_{j-1} + b_{j+1} + 16b_{j+2}) \\ \frac{1}{4!}(a_{j-1} + a_{j+1}) = \frac{1}{5!}(-32b_{j-2} - b_{j-1} + b_{j+1} + 32b_{j+2}) \\ \frac{1}{5!}(-a_{j-1} + a_{j+1}) = \frac{1}{6!}(64b_{j-2} + b_{j-1} + b_{j+1} + 64b_{j+2} + n). \end{cases} \tag{5}$$

Solving these equations, the coefficients with a free parameter n can be obtained,

$$\begin{cases} a_{j-1} = \frac{n}{12} + \frac{1}{3}, & a_{j+1} = -\frac{n}{12} + \frac{1}{3} \\ b_{j-2} = -\frac{n}{72} - \frac{1}{36}, & b_{j-1} = -\frac{n}{9} - \frac{7}{9}, & b_j = \frac{n}{4}, \\ b_{j+1} = -\frac{n}{9} + \frac{7}{9}, & b_{j+2} = -\frac{n}{72} + \frac{1}{36}. \end{cases} \tag{6}$$

Each value of the free parameter n corresponds to a specific scheme. Specially, when $n = 0$, the scheme is the sixth-order compact central scheme (sixth-CCS) proposed by Lele.¹ The coefficients of the sixth-CCS meet the requirements of $a_{j-1} = a_{j+1}$, $b_{j-1} = b_{j+1}$, and $b_{j-2} = b_{j+2}$. Thus, it is a symmetric scheme, which is non-dissipative. It will hereinafter be referred to as CCS.

If in Eq. (2) $a_{j+1} = 0$, the stencil is derivative-biased, which falls to the second type of scheme, DCUS. There are six unknowns in the DCUS, and it can reach the fifth order at most. For DCUS, the parameter n , which is the coefficients of the fifth-order term in the truncation error, is decided by other coefficients in the difference expression.

Thus, the free parameter for DCUS is m . The other coefficients of the DCUS can be obtained via m as follows:

$$\begin{cases} a_{j-1} = -\frac{m}{6} + \frac{2}{3}, & a_{j+1} = 0 \\ b_{j-2} = \frac{m}{24} - \frac{1}{12}, & b_{j-1} = \frac{5m}{36} - \frac{11}{9}, & b_j = -\frac{m}{4} + 1, \\ b_{j+1} = \frac{m}{12} + \frac{1}{3}, & b_{j+2} = -\frac{m}{72} - \frac{1}{36}. \end{cases} \tag{7}$$

When $m = 0$, the scheme is the fifth-order compact upwind scheme proposed by Fu and Ma,¹⁴ which will hereinafter be called as SDCUS. If $m = 4$, the scheme is the fourth-order spatial-explicit central scheme.

If in Eq. (2) $b_{j+2} = 0$, the stencil is function-biased, and the corresponding scheme is the FCUS. The following are the coefficients of the FCUS:

$$\begin{cases} a_{j-1} = -\frac{m}{4} + \frac{1}{2}, & a_{j+1} = \frac{m}{12} + \frac{1}{6} \\ b_{j-2} = \frac{m}{18} - \frac{1}{18}, & b_{j-1} = \frac{m}{4} - 1, & b_j = -\frac{m}{2} + \frac{1}{2}, \\ b_{j+1} = \frac{7m}{36} + \frac{5}{9}, & b_{j+2} = 0. \end{cases} \tag{8}$$

When $m = 0$, the scheme is the fifth-order standard compact upwind scheme (fifth-SCUS) proposed by Fan,²¹ which will be hereinafter called as SFCUS. If $m = 1$, the scheme is the fourth-order compact central scheme (fourth-CCS) proposed by Lele.¹

B. Spatial resolution of the compact schemes

To quantitatively evaluate the error characteristics of these compact schemes mentioned above, the first-order wave equation (advection equation) is analyzed by the Fourier analysis:

$$\frac{\partial u}{\partial t} + c \frac{\partial u}{\partial x} = 0, \quad c > 0, \tag{9}$$

where c is the constant phase speed. The Fourier transform of the solution is shown in the following equation:

$$u(x, t) = \int \hat{u}(k, t) e^{ikx} dk, \tag{10}$$

where i represents the imaginary unit, $i = \sqrt{-1}$; k is the wavenumber, which denotes the scales of the motion in flow problem, and high wavenumbers correspond to small scales. The accurate first-order derivative of $u(x, t)$ is

$$\frac{\partial u}{\partial x} = \int ik \hat{u}(k, t) e^{ikx} dk. \tag{11}$$

While for the finite difference method, the discrete first-order derivative can be expressed as

$$u' = \int ik_{eq} \hat{u}(k, t) e^{ikx} dk, \tag{12}$$

where k_{eq} is the modified wavenumber. It can be seen from Eqs. (11) and (12) that if $k_{eq} = k$, there would be no error for the difference

approximation; therefore, the modified wavenumber k_{eq} is a criterion to evaluate the error of difference approximation.

Substituting Eqs. (10) and (12) in the difference expression [Eq. (3)], Eq. (13) is obtained, and the formula to calculate the modified wavenumber is shown in the following equation:

$$ik_{eq}\hat{u}(a_{j-1}e^{-ix} + 1 + a_{j+1}e^{-ix}) = \frac{1}{h}\hat{u}(b_{j-2}e^{-i2x} + b_{j-1}e^{-ix} + b_j + b_{j+1}e^{ix} + b_{j+2}e^{i2x}), \quad (13)$$

$$k_{eq} = -i\frac{1}{h}\frac{(b_{j-2}e^{-i2x} + b_{j-1}e^{-ix} + b_j + b_{j+1}e^{ix} + b_{j+2}e^{i2x})}{(a_{j-1}e^{-ix} + 1 + a_{j+1}e^{-ix})}, \quad (14)$$

where $\alpha = kh$ is the scaled wavenumber. Obviously, the modified wavenumber is a complex function of scaled wavenumber, which can be written as

$$k_{eq}(\alpha) = k_r(\alpha) + ik_i(\alpha), \quad (15)$$

where $k_r(\alpha)$ and $k_i(\alpha)$ represent the real part and the imaginary part of the modified wavenumber, respectively.

Assuming that the temporal approximation is accurate enough, the exact solution and numerical solution of Eq. (9) with the initial condition, Eq. (16), are represented in the following equations:

$$u(x, 0) = \int \hat{u}(k, 0)e^{ikx} dk, \quad (16)$$

$$u(x, t) = \int \hat{u}(k, 0)e^{ik(x-ct)} dk, \quad (17)$$

$$u(x, t) = \int \hat{u}(k, 0)e^{k_i(\alpha)ct} e^{ik(x-\frac{k_r(\alpha)}{k}ct)} dk. \quad (18)$$

The numerical solution is equivalent to the exact solution only if the modified wavenumber satisfies the following conditions:

$$\frac{k_r(\alpha)}{k} = 1, \quad (19)$$

$$k_i(\alpha) = 0. \quad (20)$$

It can be observed from the comparison between Eqs. (17) and (18) that the real part of the modified wavenumber k_r relates to the error in phase, while the imaginary part k_i relates to the error in amplitude. The amplitude error is called the dissipation error, and the phase error is called the dispersion error. To get an unified non-dimensional expression, Eqs. (19) and (20) can be rewritten as the following equations:

$$k_r(\alpha)h = \alpha, \quad (21)$$

$$k_i(\alpha)h = 0. \quad (22)$$

Thus, the error characteristics can be evaluated by the scaled modified wavenumber $k_{eq}h$.

The error characteristics for the standard form of the three types of compact upwind schemes are analyzed with the Fourier analysis. The scheme with the free parameter being set to zero is the standard form, which has the highest order of its type. The standard forms of CCUS, FCUS, and DCUS are the CCS, SFCUS, and SDCUS, respectively, mentioned in Sec. II A. The difference expressions of the three standard schemes are shown in the following equations:

CCS:

$$\frac{1}{3}u'_{j-1} + u'_j + \frac{1}{3}u'_{j+1} = \frac{1}{36h}(-u_{j-2} - 28u_{j-1} + 28u_{j+1} + u_{j+2}). \quad (23)$$

SFCUS:

$$\frac{1}{2}u'_{j-1} + u'_j + \frac{1}{6}u'_{j+1} = \frac{1}{18h}(-u_{j-2} - 18u_{j-1} + 9u_j + 10u_{j+1}). \quad (24)$$

SDCUS:

$$\frac{2}{3}u'_{j-1} + u'_j = \frac{1}{36h}(-3u_{j-2} - 44u_{j-1} + 36u_j + 12u_{j+1} - u_{j+2}). \quad (25)$$

It should be noted that the standard form of CCUS is not of upwind-type scheme. It is widely adopted in the literature, hence listed here as a reference scheme and termed it CCS rather than SCCUS.

The scaled wavenumbers of these three compact schemes are shown in Fig. 1. In Fig. 1(a), the line $k_i h = 0$ represents the exact solution that is non-dissipative, and the deviations of other curves from it represents the dissipation error. In Fig. 1(b), the dashed line $k_r h = \alpha$ represents the exact solution without dispersion error, and the deviations of other curves from it represents the dispersion error. In Fig. 1(a), the dissipation error of CCS equals zero over the whole wavenumber range; thus, the amplitude term $e^{k_i(\alpha)ct}$ in Eq. (18) is identical to one. Comparing Eqs. (17) and (18), it can be found that the amplitude of the solution for all scales will be completely preserved. For SFCUS and SDCUS, the low-dissipative region is restricted to the low-wavenumber part, and in the high-wavenumber part, both compact upwind schemes have high dissipation errors. These characteristics indicate that only the amplitude of solution for low wavenumbers can be retained and the small-scale structures, which correspond to high wavenumbers will be dissipated. The SFCUS, which has a wider range of low dissipation than the SDCUS, can resolve more scales than SDCUS. On the other hand, from Fig. 1(b), it can be seen that the dispersion errors of all three schemes in the high wavenumber region are large, which means that the solution of small scales has incorrect speeds and will finally result in numerical instability.

To evaluate the error characteristics of these schemes quantitatively, the maximum resolution wavenumber α_m is employed here as a reference. Once the tolerance is given, the maximum resolution wavenumber α_m for the dispersion error is the maximum scaled wavenumber that satisfies

$$\frac{|k_r(\alpha)h - \alpha|}{\alpha} < \varepsilon, \quad (26)$$

while for the dissipation error, the requirement is

$$-k_i(\alpha)h < \varepsilon. \quad (27)$$

From Eqs. (26) and (27), it is known that the maximum resolution wavenumber represents the wavenumber range of low dissipation or low dispersion under a specific tolerance. For example, if the tolerance is set to 1%, the dissipation or dispersion error can be limited under 1% for the wavenumber smaller than α_m . Therefore, a scheme with a higher α_m is preferable.

The maximum resolution wavenumbers of the three standard schemes under the tolerance of 0.5% and 0.1% are listed in Table I. As mentioned above, the CCS is non-dissipative, and thus, its maximum resolution wavenumber for low dissipation is π . Apart from the CCS,

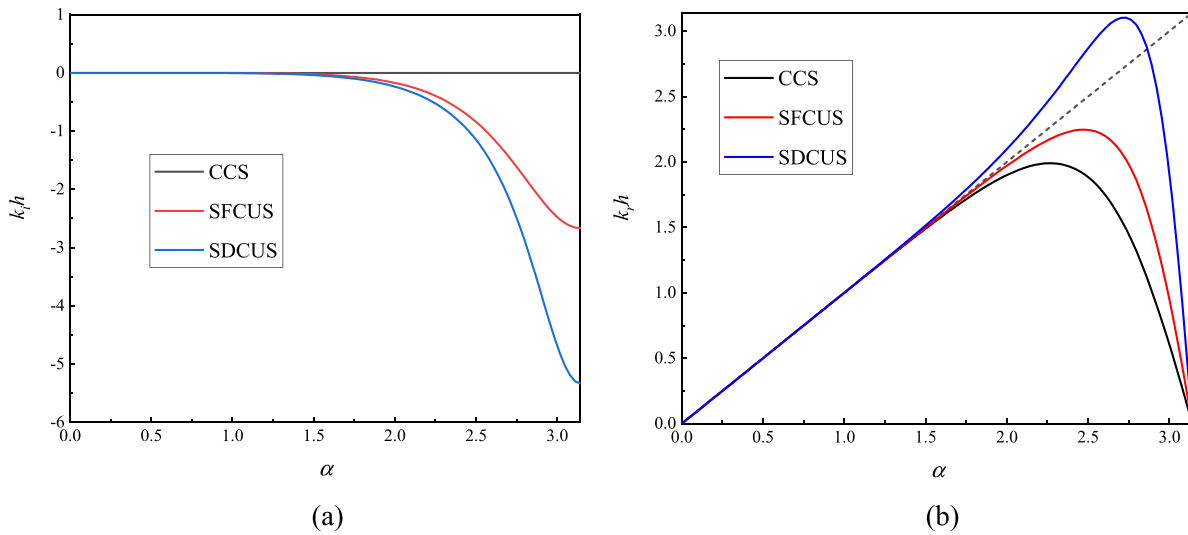


FIG. 1. Scaled modified wavenumber of the standard schemes: (a) the imaginary part and (b) the real part.

the values of α_m for low dissipation of the other two schemes are smaller due to their inherent dissipation. The maximum resolution wavenumber of these schemes for low dispersion are all smaller than π , which indicates that the dispersion error is inevitable in the high wavenumber region. In addition, whether the tolerance is 0.5% or 0.1%, the SFCUS has the highest resolution for low dispersion among these three schemes, and its dissipation error is less than that of the SDCUS. From the results of Fourier analysis, the SFCUS is superior to the SDCUS.

III. THE PROPOSED OPTIMIZATION METHOD OF THE COMPACT UPWIND SCHEME

In Sec. II, the three types of compact upwind schemes with different stencils are introduced. The spatial resolution of the standard schemes, which have the highest order of each type of scheme, is compared. It should be noticed that the scheme with high order does not necessarily have better resolution characteristics. Improving the resolution characteristics of the schemes can capture smaller flow features on the same mesh and get more accurate wave propagation speeds. Therefore, in this section, an optimization method is proposed to optimize the coefficient of the three types of compact upwind schemes to improve the dispersion and dissipation characteristics at the same time.

TABLE I. The maximum resolution wavenumber of the standard schemes for two tolerances.

α_m	$-k_i h < 0.5\%$	$\frac{ k_r h - \alpha }{\alpha} < 0.5\%$	$-k_i h < 0.1\%$	$\frac{ k_r h - \alpha }{\alpha} < 0.1\%$
CCS	π	1.42	π	1.10
SFCUS	1.21	1.73	0.89	1.35
SDCUS	1.08	1.35	0.79	1.03

A. Dispersion-dissipation-balancing optimization method

The scheme with dissipation error can effectively eliminate the oscillations resulting from the dispersion error. However, the excessive dissipation error will also dissipate the small-scale structures. A proper range of dissipation error cannot only dissipate the nonphysical oscillations but also retain the small scales as much as possible, which requires that the dispersion error and dissipation error should be balanced. Thus, the dispersion-dissipation-balancing optimization (DDB) method is proposed in this section.

The DDB optimization is to find the optimal free parameters m or n in Eq. (2), with which the schemes obtained satisfies

$$\alpha_{m,disp} = \alpha_{m,diss}, \tag{28}$$

where $\alpha_{m,disp}$ and $\alpha_{m,diss}$ are the maximum resolution wavenumbers that satisfy Eqs. (26) and (27) under a given tolerance ϵ , respectively. Large $\alpha_{m,disp}$ represents large wavenumber range of low dispersion, and large $\alpha_{m,diss}$ represents large wavenumber range of low dissipation.

The value range of the free parameters m and n should be determined. Figure 2 shows the corresponding maximum resolution wavenumbers when the tolerance in Eqs. (26) and (27) is 0.1%. In the figure, the value on the abscissa is the free parameter that represents a specific scheme, and the value on the ordinate is the maximum resolution wavenumber, whose value represents the resolution of the scheme. The blue line represents $\alpha_{m,disp}$, and the red line represents $\alpha_{m,diss}$. Taking Fig. 2(a) as an example, $n = 0$ corresponds to the CCS, of which the dissipation error is always zero. No matter how small the tolerance value is, Eq. (27) can be satisfied in the whole wavenumber range, so the maximum resolution wavenumber is π . When $n < 0$, the maximum wavenumber that satisfies Eq. (27) is 0. It can be known from Eqs. (6) and (14) that $k_i h$ for CCUS is a continuous function with $k_i h(0) = 0$. Therefore, the value of $k_i h$ must be larger than zero for all wavenumbers. When $k_i h > 0$, the amplitude term $e^{k_i(\alpha)ct}$ in the

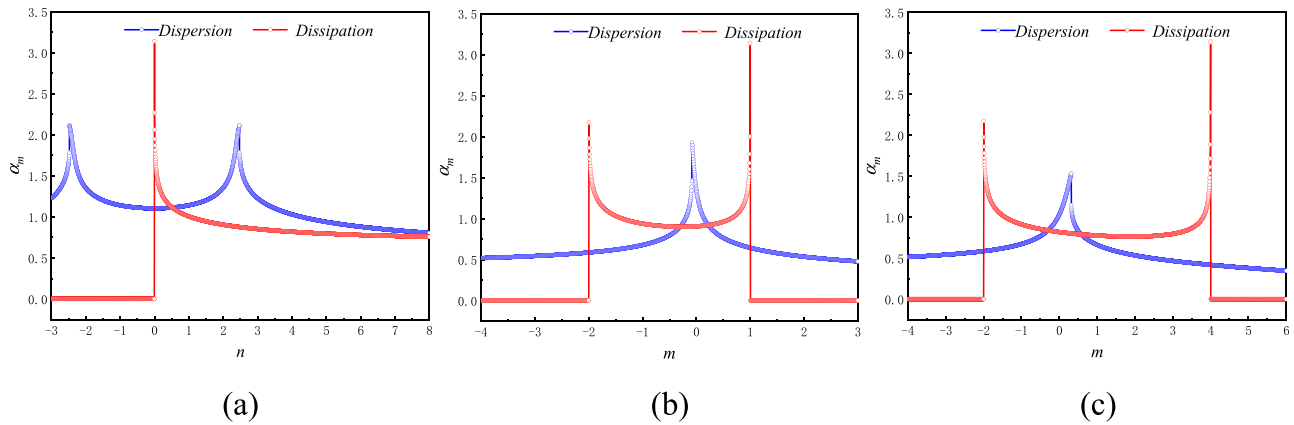


FIG. 2. The maximum resolution wavenumbers of (a) CCUS, (b) FCUS, and (c) DCUS.

numerical solution [Eq. (18)] will gradually grow up as time goes on, eventually leading to divergence. This property is called anti-dissipation. Consequently, the scheme with positive imaginary part of the scaled modified wavenumber ($k_r h > 0$) is unstable. When $n > 0$, $0 < \alpha_{m,diss} < \pi$, the scheme is dissipative. It can be concluded that the CCUS is an upwind scheme only when $n > 0$. Similarly, the FCUS is an upwind scheme under the condition of $-2 < m < 1$, and for the DCUS, the upwind requirement is $-2 < m < 4$. Figure 3 presents the imaginary part of the scaled modified wavenumber for different schemes. As shown in the figure, apart from the three standard compact schemes, the other five kinds of schemes of which the free parameter is out of the upwind range all have positive $k_r h$, which means the anti-dissipation as previously stated. So, all these five schemes cannot be stable. As a consequence, during the optimization process, the range of the free parameters must meet the upwind requirements. Finding

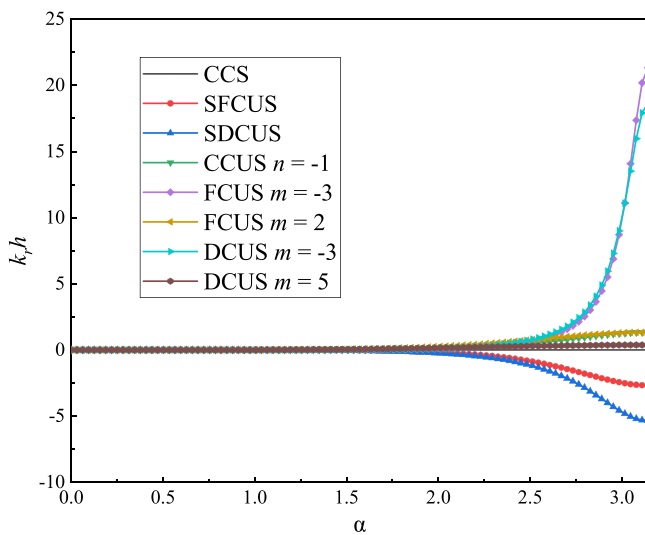


FIG. 3. The imaginary part of the scaled modified wavenumber for different schemes.

the upwind range in advance can greatly reduce the workload of optimization and avoid the schemes with anti-dissipation.

It can also be found in Fig. 2 that in the upwind region for a specific type of scheme, the dispersion error (blue lines) and the dissipation error (red lines) are often mismatched, that is, the scheme with a lower dispersion error often has a higher dissipation error. Whether the dispersion error is large or the dissipation error is large, the numerical solution is inaccurate. It is reasonable to keep the small dispersion error and dissipation error in the widest possible wavenumber region, which is the original intention for the DDB optimization method.

The tolerance of the DDB optimization method in this paper is selected as 0.5%. After optimization, the values of the optimal free parameter determined for CCUS, FCUS, and DCUS are $n = 1/2$, $m = 1/3$, and $m = -7/15$, respectively. The corresponding coefficients and the maximum resolution wavenumbers of the three DDB-optimized schemes are listed in Tables II and III, respectively.

The spectral performance of the DDB-optimized schemes will be tested in Sec. III B. In the optimization strategy proposed by Tam and Webb,²⁹ spatial and temporal discretization is considered simultaneously. However, the temporal derivative was discretized by a five-time-level method, bringing three extra spurious modes. To avoid these spurious modes, the third-order Runge–Kutta method is adopted for temporal discretization in the present study.

For comparison purposes, the popular DRP optimization method is adopted here. As mentioned in Sec. I, the main idea of DRP optimization is to maintain the dispersion relation at a relatively wider wavenumber region, and the optimization is often carried out with only the real part of the modified wavenumber. In this work, to determine the DRP coefficients, the second method of implementation in Ref. 38 is adopted. The optimal free parameter for CCUS is $n = 2.460$, and for FCUS and DCUS, the optimal parameters are $m = -0.080$ and $m = 0.318$, respectively. The coefficients of these three DRP schemes are listed in Table IV.

B. Spectral analysis of the compact upwind schemes

The spectral analysis method for scheme performance analysis is proposed by Sengupta and Ganerival² and improved in Refs. 39 and 40. It analyzes the error characteristics for both spatial and temporal discretization. For a better explanation, the same governing equation

TABLE II. Coefficients of DDB-optimized schemes ($u_j > 0$).

Scheme	a_{j-1}	a_{j+1}	b_{j-2}	b_{j-1}	b_j	b_{j+1}	b_{j+2}
OCCUS_DDB	0.375	0.291 67	-0.034 72	-0.833 33	0.125	0.722 22	0.020 83
OFCUS_DDB	0.416 67	0.194 44	-0.037 04	-0.916 67	0.833 33	0.620 37	0
ODCUS_DDB	0.744 44	0	-0.102 78	-1.287 04	1.116 67	0.294 44	-0.0213

TABLE III. The maximum resolution wavenumber of DDB-optimized schemes under the tolerance of 0.5%.

α_m	$-k_j h < 0.5\%$	$\frac{ k_r h - \alpha }{\alpha} < 0.5\%$
OCCUS_DDB	1.43	1.43
OFCUS_DDB	1.21	1.21
ODCUS_DDB	1.11	1.11

[Eq. (9)] is analyzed here, and the first-order Euler scheme is adopted for the temporal discretization,

$$\frac{u_j^{n+1} - u_j^n}{\Delta t} = -c\delta_x u_j, \tag{29}$$

where $\delta_x u_j$ is the difference approximation of $\partial u / \partial x$. Taking the Fourier transform of the space-time independent variable $u(x, t)$ shown in Eq. (10), and bringing it into Eq. (29), the following equation is obtained:

$$\frac{\hat{u}(k, t + \Delta t) - \hat{u}(k, t)}{\Delta t} = -c \frac{1}{h} (ik_{eq} h) \hat{u}(k, t). \tag{30}$$

Defining the amplification factor as $G = \hat{u}(k, t + \Delta t) / \hat{u}(k, t)$, Eq. (30) can be transformed to

$$G = 1 - Cr(ik_{eq} h), \tag{31}$$

where $Cr = \frac{c\Delta t}{h}$ is the Courant number. Obviously, G is also a complex quantity, and it is a function of Cr and α : $G(Cr, \alpha) = G_r(Cr, \alpha) + iG_i(Cr, \alpha)$.

With the amplification factor and the initial condition [Eq. (16)], the numerical solution of Eq. (9) can be easily obtained,

$$\begin{aligned} u(x, t) &= u(x, n\Delta t) = \int \hat{u}(k, 0) G^n(k) e^{ikx} dk \\ &= \int \hat{u}(k, 0) |G|^n e^{i(kx - n\beta)} dk, \end{aligned} \tag{32}$$

where $|G|$ is the magnitude of amplification factor: $|G| = (G_r^2 + G_i^2)^{\frac{1}{2}}$. If $|G| = 1$, there is no dissipation error in the spatiotemporal

TABLE IV. Coefficients of DRP schemes.

Scheme	a_{j-1}	a_{j+1}	b_{j-2}	b_{j-1}	b_j	b_{j+1}	b_{j+2}
OCCUS_DRP	0.538 33	0.128 33	-0.061 94	-1.051 11	0.615	0.504 44	-0.006 39
OFCUS_DRP	0.52	0.16	-0.06	-1.02	0.54	0.54	0
ODCUS_DRP	0.613 67	0	-0.070 08	-1.178 06	0.9205	0.359 83	-0.032 19

discretization. $n\beta$ is the argument with $\tan \beta = -G_i / G_r$, which is the phase shift of the numerical solution that relates to dispersion error. To better describe the dispersion error, the numerical group velocity $V_{g,N}$ is introduced. The group velocity is the velocity that the energy of a convective system travels with Ref. 39. For the problem defined in Eq. (9), the physical group velocity equals the phase velocity c . Therefore, if $V_{g,N} = c$, there is no dispersion error in the spatiotemporal discretization. In addition, the region where $V_{g,N} < 0$ is prone to q -waves, which are nonphysical waves.⁴¹ The q -waves have short wavelengths and usually propagate against the physical velocity. They are often manifested as nonphysical oscillations, significantly impact the results, and even lead to divergence. The nondimensional numerical group velocity defined by $\frac{V_{g,N}}{c}$ can be obtained by

$$\frac{V_{g,N}}{c}(Cr, \alpha) = \frac{1}{c} \frac{d\beta / \Delta t}{dk} = \frac{1}{Cr} \frac{d\beta}{d\alpha}. \tag{33}$$

Next, the spectral analysis is applied to the compact upwind schemes mentioned above. The attention is focused on the magnitude of the amplification factor and numerical group velocity, which represents the dissipation error and the dispersion error, respectively. The temporal discretization adopts the third-order Runge-Kutta method proposed in Ref. 42. For this method, the amplification factor can be computed by the following equation:

$$G = 1 - A + \frac{A^2}{2} - \frac{A^3}{6}, \tag{34}$$

where $A = Cr(ik_{eq} h)$.

Figures 4 and 5 show the magnitude of the amplification factor ($|G|$) and the dimensionless numerical group velocity ($V_{g,N}/c$) for three kinds of CCUSs, respectively. In Fig. 4, the values shown by the board number and attached to each curve are the values of $|G|$. The hatched region at the left bottom corner is the neutrally stable region where the magnitude of the amplification factor equals one. In this region, the solution will not be amplified or attenuated. In Fig. 4(a), when $Cr < 0.014$, $|G| = 1$, and the CCS is neutrally stable for all wavenumbers. If $0.014 < Cr < 0.871$, this scheme shows little dissipation but is still stable. If $Cr > 0.871$, the amplification is larger than 1, which means that the solution will be amplified with time, finally leading to divergence in long-time integration. The CCS is no longer stable when

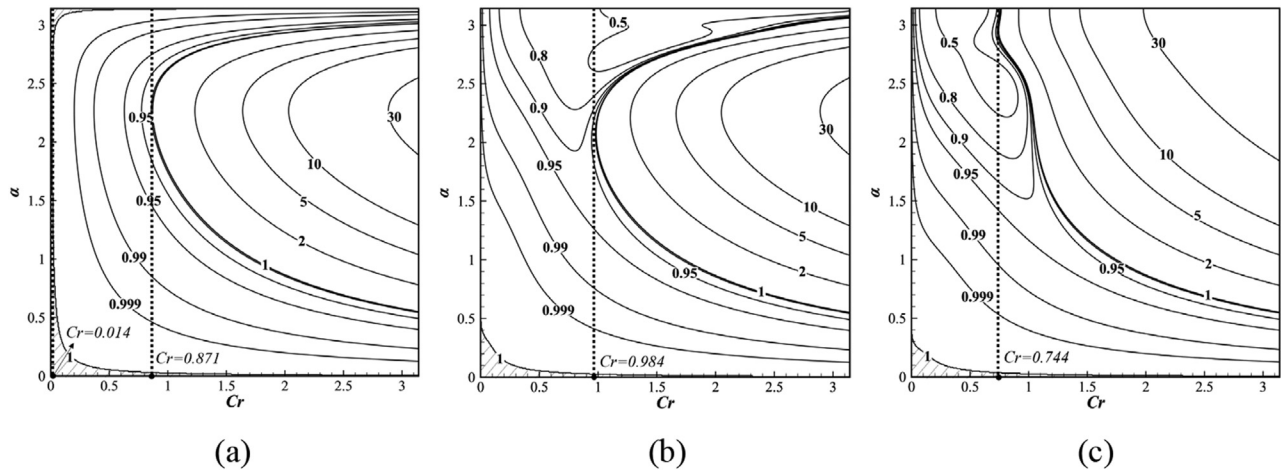


FIG. 4. The magnitude of amplification factor ($|G|$) of three CCUSs: (a) CCS, (b) OCCUS_DDB, and (c) OCCUS_DRP.

$Cr > 0.871$, so the critical Cr for the CCS is 0.871. For the two optimized compact upwind schemes in Figs. 4(b) and 4(c), the neutrally stable region is restricted to an area of low wavenumber and small Cr . Even for a very small Cr , the schemes are dissipative at the high-wavenumber region. Compared with the ODCUS_DRP, the OCCUS_DDB, whose critical Cr is 0.984, has a larger area of stability. In addition, the dissipation error of the OCCUS_DDB is smaller than OCCUS_DRP in the stable region.

In Fig. 5, the values shown by the board number and attached to each curve are the values of dimensionless numerical group velocity. Here, attention should be paid to two regions. One is the region where the dimensionless numerical group velocity is less than 0, and the other is the DRP region where the dimensionless numerical group velocity is close to 1. In the region with negative group velocity, the q -waves will appear and interfere with the numerical results. When Cr is

small, all three schemes have negative group velocities in the high wavenumber region. Only the OCCUS_DRP have the opposite group velocity for all wavenumber range at large Cr . Still, the corresponding Cr is larger than the critical Cr , which is determined to be unstable in Fig. 4. Consequently, it seems that all schemes cannot avoid the q -waves. On the other hand, in the DRP region, the dispersion error is small. It is undeniable that all three schemes have nonnegligible dispersion errors. Among these schemes, the OCCUS_DRP has the best dispersion characteristics. When Cr is small, the OCCUS_DRP has the largest wavenumber range of low dispersion error and the smallest wavenumber range of negative numerical group velocity. It is not difficult to understand. After all, the original intention of the DRP schemes is to minimize the dispersion error as much as possible, and it will correspondingly reduce the requirement of dissipation error.

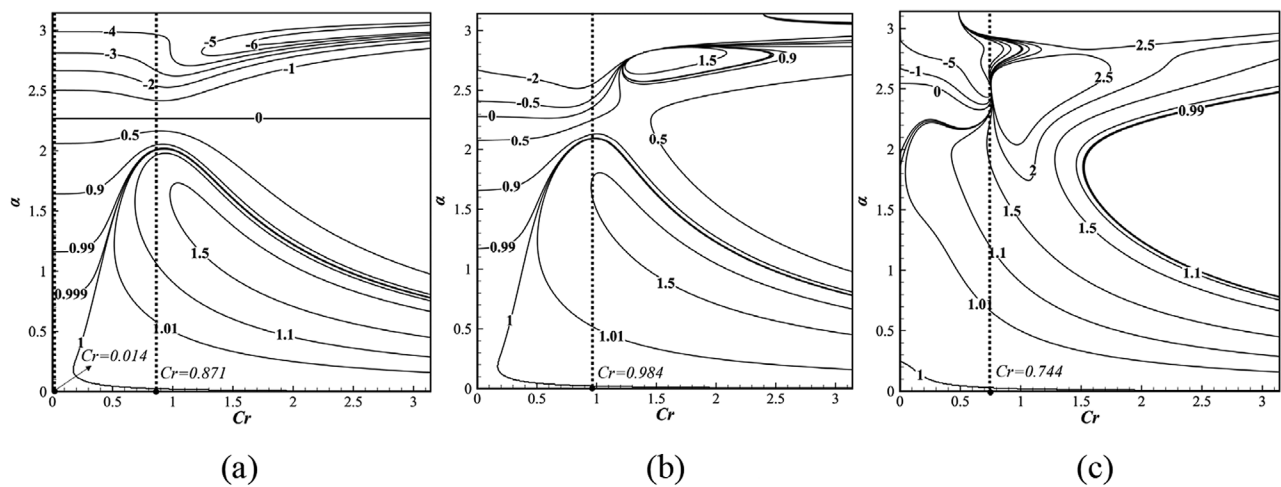


FIG. 5. The dimensionless numerical group velocity ($V_{g,N}/c$) of three CCUSs: (a), CCS (b) OCCUS_DDB, and (c) OCCUS_DRP.

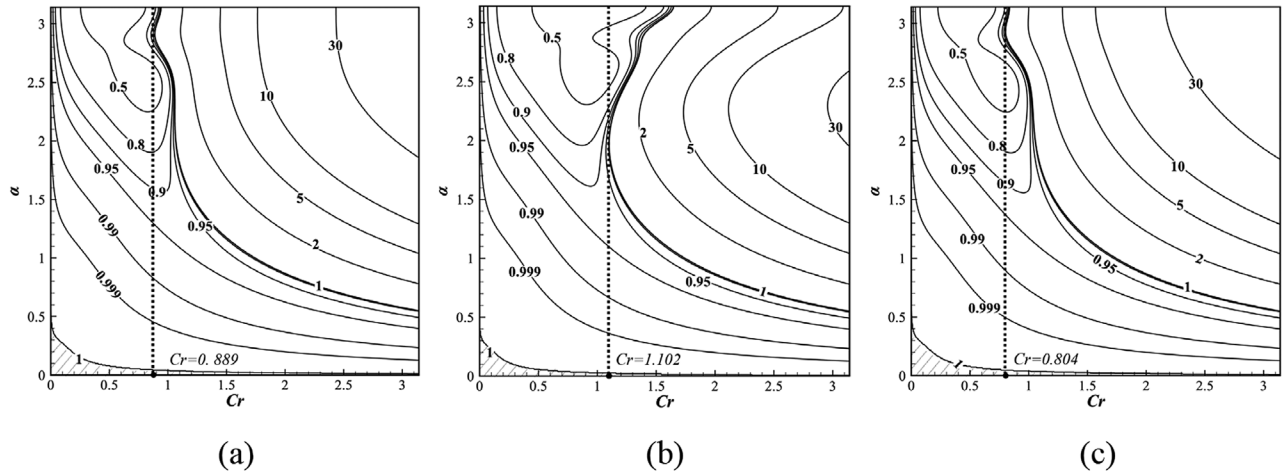


FIG. 6. The magnitude of amplification factor ($|G|$) of three FCUSs: (a) SFCUS, (b) OFCUS_DDB, and (c) OFCUS_DRP.

The error characteristics of FCUSs are shown in Figs. 6 and 7. Due to the asymmetric stencil, the three FCUSs are all upwind schemes. They do not have the all-wavenumber-range neutrally stable region. The same phenomenon can be found in Figs. 8 and 9 for the DCUSs, which also use the biased stencil. For FCUS, the DDB optimized scheme has the largest stable range and the smallest dissipation error. However, for DCUS, the DDB optimized scheme does not have the best stability properties anymore. It may result from the strong inherent dissipation of the derivative-biased stencil. It will cost more to balance the dispersion and dissipation error, so the final balance point is at a low-resolution position. Thus, the DDB optimization method is not suitable for DCUS. Furthermore, it should be noted that for both the standard and the optimized schemes, no matter which optimization method is used, the FCUSs are superior to the DCUSs for both stability and error characteristics.

In the following, the characteristics of OCCUS_DDB and OCCUS_DRP are compared in detail by applying them to solve the 1D wave equation.

C. Solving 1D wave equation

In Sec. III B, the error characteristics are evaluated by a spatio-temporal spectral analysis. In this subsection, the propagation of a steep ramp signal following the 1D wave equation [Eq. (9)] is studied to explain the results.

The computational domain is $-15 \leq x \leq 45$, which is discretized by 8192 uniform-arranged points. At the initial time, the ramp signal with a slope of 6 starts from $x=14$ and ends at $x=15$. The phase velocity is chosen as $c=0.5$, and the images of the ramp signal at $t=0, 3, 6$ are plotted in Fig. 10. The third-order Runge-Kutta method is used for time advancing, and the three CCUSs are used for spatial discretization. The simulation is conducted under different Cr , and the stability properties of three CCUSs obtained by the spectral analysis are listed in Table V. Considering that the amplitude of the error is small compared with the ramp signal when Cr is small, only the distributions of the error defined as the difference between the exact solution and the numerical solution are discussed.

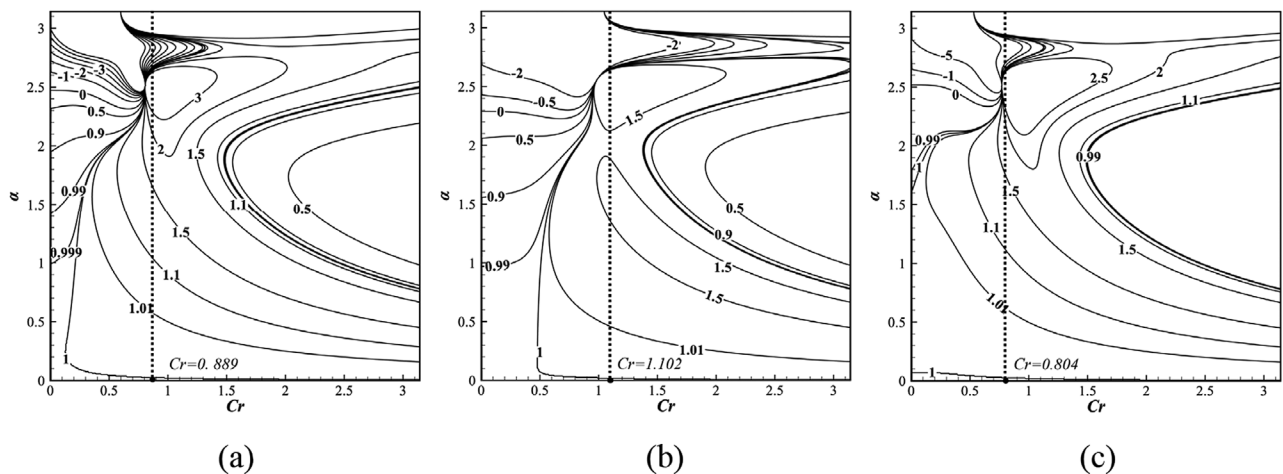


FIG. 7. The dimensionless numerical group velocity ($V_{g,N}/c$) of three FCUSs: (a) SFCUS, (b) OFCUS_DDB, and (c) OFCUS_DRP.

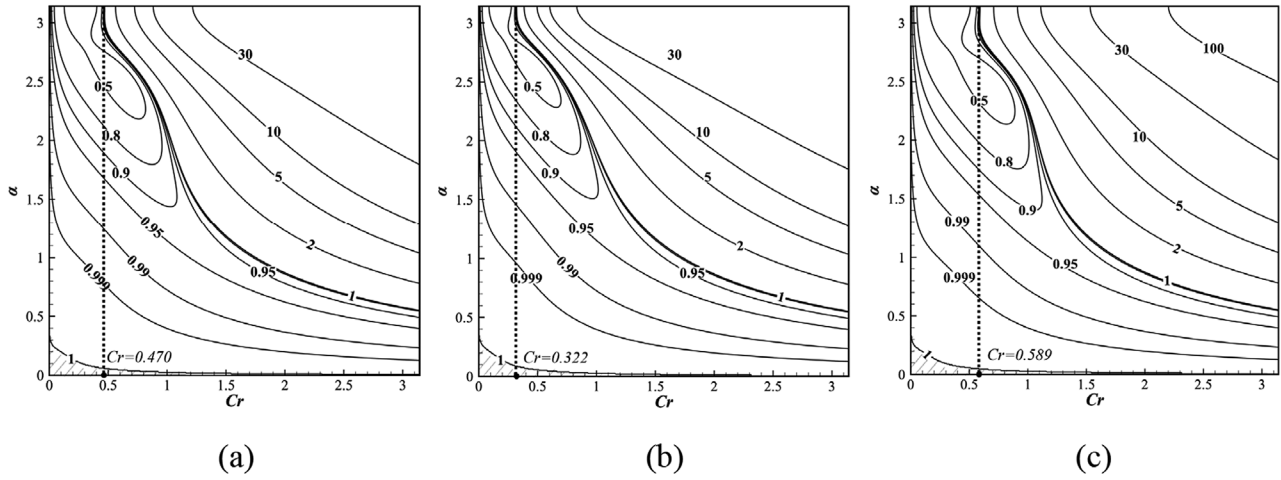


FIG. 8. The magnitude of amplification factor ($|G|$) of three DCUSs: (a) SDCUS, (b) ODCUS_DDB, and (c) ODCUS_DRP.

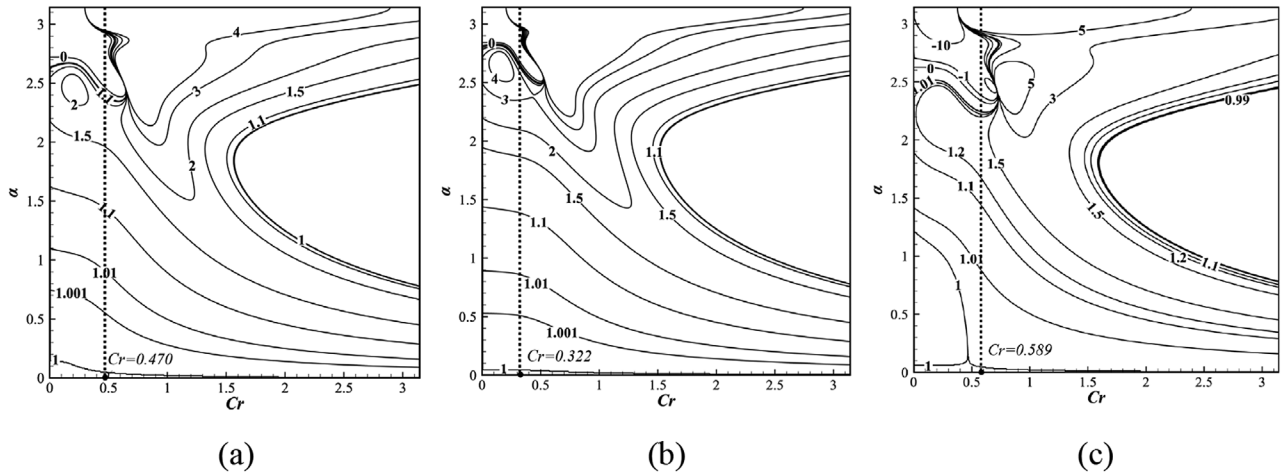


FIG. 9. The dimensionless numerical group velocity ($V_{g,N}/c$) of three DCUSs: (a) SDCUS, (b) ODCUS_DDB, and (c) ODCUS_DRP.

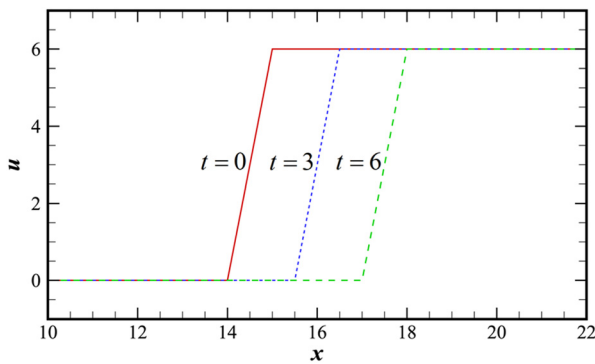


FIG. 10. The propagation of a steep ramp signal.

Figure 11 shows the errors of the numerical solution by the three schemes when $Cr = 0.01$. From the spectral analysis results, the CCS is neutrally stable for all wavenumbers since $Cr < 0.014$. The amplitude of the solution obtained by CCS should have been unchanged. However, Fig. 11(a) shows severe spurious waves propagating along the opposite direction of the ramp signal. As previously stated, these

TABLE V. The stability of three CCUSs at different Cr obtained by spectral analysis.

Cr	0.01	0.252	0.768	0.975
CCS	Neutrally stable	Dissipative	Dissipative	Unstable
OCCUS_DDB	Dissipative	Dissipative	Dissipative	Dissipative
OCCUS_DRP	Dissipative	Dissipative	Unstable	Unstable

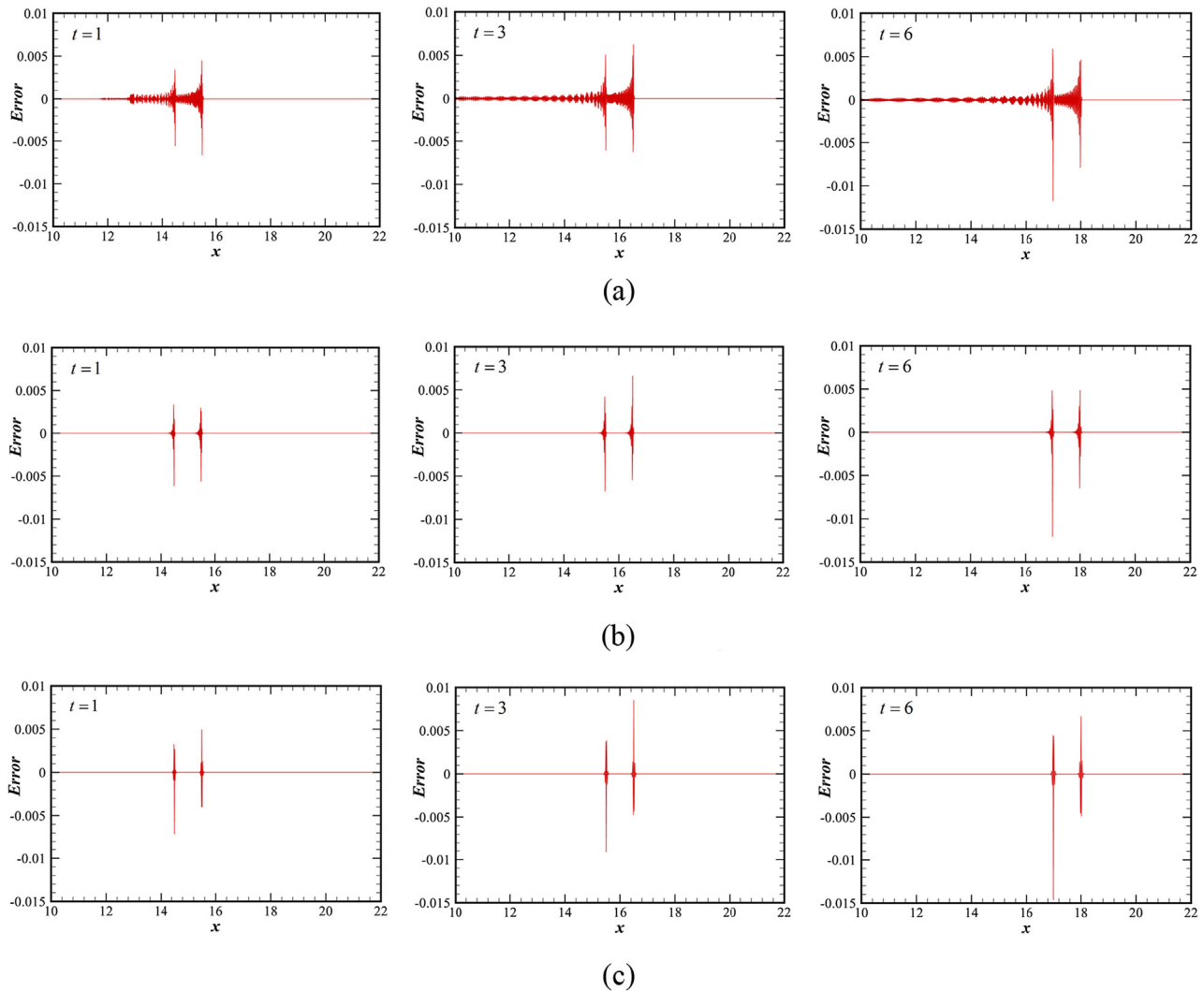


FIG. 11. The errors of three CCUSs for $Cr = 0.01$: (a) CCS, (b) CCUS_DDB, and (c) CCUS_DRP.

spurious waves are q -waves that result from negative numerical group velocities. On the one hand, for all schemes mentioned in this paper, the numerical group velocities at the high wavenumber range are all negative when Cr is small. On the other hand, Cr cannot be too large to ensure stability. Thus, the q -waves seem inevitable at the high-wavenumber region for all schemes. However, as shown in Figs. 11(b) and 11(c), these spurious waves do not appear in the solutions by OCCUS_DDB and OCCUS_DRP. It is precisely because the upwind schemes like OCCUS_DDB and OCCUS_DRP have inherent dissipation in the high wavenumber range that can attenuate the q -waves. Since the q -waves will draw energy from the exact solution, leading to nonphysical results and numerical instability, adding proper dissipation to suppress the q -waves is beneficial for the numerical simulation. In addition, although it is not very obvious, it is worth noting that the amplitude of the error for OCCUS_DDB is smaller than

OCCUS_DRP from the comparison of Figs. 11(b) and 11(c), which reflects the advantage of OCCUS_DDB.

If Cr increases to 0.252, the CCS is not neutrally stable but dissipative. The number of q -waves in Fig. 12(a) is fewer than that in Fig. 11(a), and it gradually decreases with time. If Cr increases to 0.768, the q -waves almost disappear due to the increased dissipation. It reveals again that the dissipation in the high wavenumber region can effectively attenuate the nonphysical q -waves. From the discussion in Sec. III B, the values of critical stable Cr for the CCS, OCCUS_DDB, and OCCUS_DRP are 0.871, 0.984, and 0.744, respectively. For the OCCUS_DRP, when $Cr = 0.768$, the magnitude of the amplification factor at a portion of wavenumbers is larger than 1. The amplitude of the waves with the corresponding wavenumber will be enlarged with time. Consequently, as shown in Fig. 13(c), the amplitude of the error for OCCUS_DRP at $t = 1$ is much larger than that of the ramp signal,

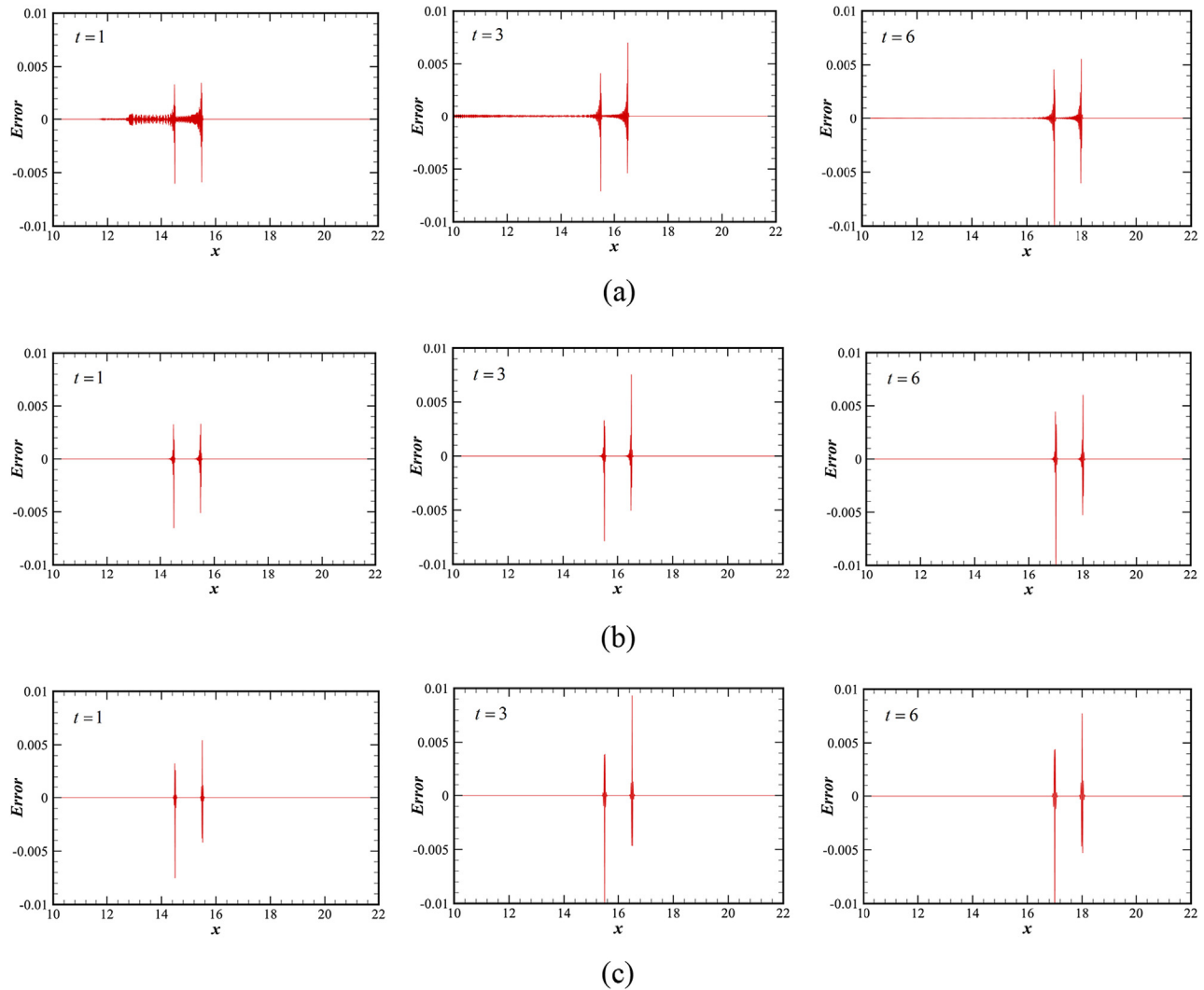


FIG. 12. The errors of three CCSUs for $Cr = 0.252$: (a) CCS, (b) CCUS_DDB, and (c) CCUS_DRP.

finally leading to the divergence of the simulation. For CCS, when $Cr = 0.975$, the error in Fig. 14(a) is also abnormally large and even increases to the order of 10^8 at $t = 3$. These phenomena are in accordance with the stability results from the spectral analysis presented in Table V.

From what mentioned above, all the schemes in this paper will theoretically generate the q -waves, and the scheme that is neutrally stable for the whole wavenumber range suffers much from the q -waves. On the contrary, the scheme with dissipation in the high wavenumber region can suppress the q -waves effectively. In addition, for CCUS and FCUS, the scheme optimized by DDB has the largest range of stability, which can help increase the time step and reduce the computation time. When solving the 1D wave equation with a ramp signal, the CCUS optimized by the DDB method is the most accurate and stable scheme in this study.

IV. PERFORMANCE COMPARISON OF NINE SCHEMES BY TWO TYPICAL FLOW PROBLEMS

In this section, Taylor Green vortex and double shear layers flow, two typical cases of unsteady incompressible flow, are employed to test the performance of the three standard compact upwind schemes (CCS, SFCUS, and SDCUS), three DDB-optimized compact upwind schemes (OCCUS_DDB, OFCUS_DDB, and ODCUS_DDB), and three DRP optimized schemes (OCCUS_DRP, OFCUS_DRP, and ODCUS_DRP) are compared.

A. Numerical model and discretization method

The Taylor Green vortex and the double shear layers flow can be described by the dimensionless continuity equation and momentum equation as follows:

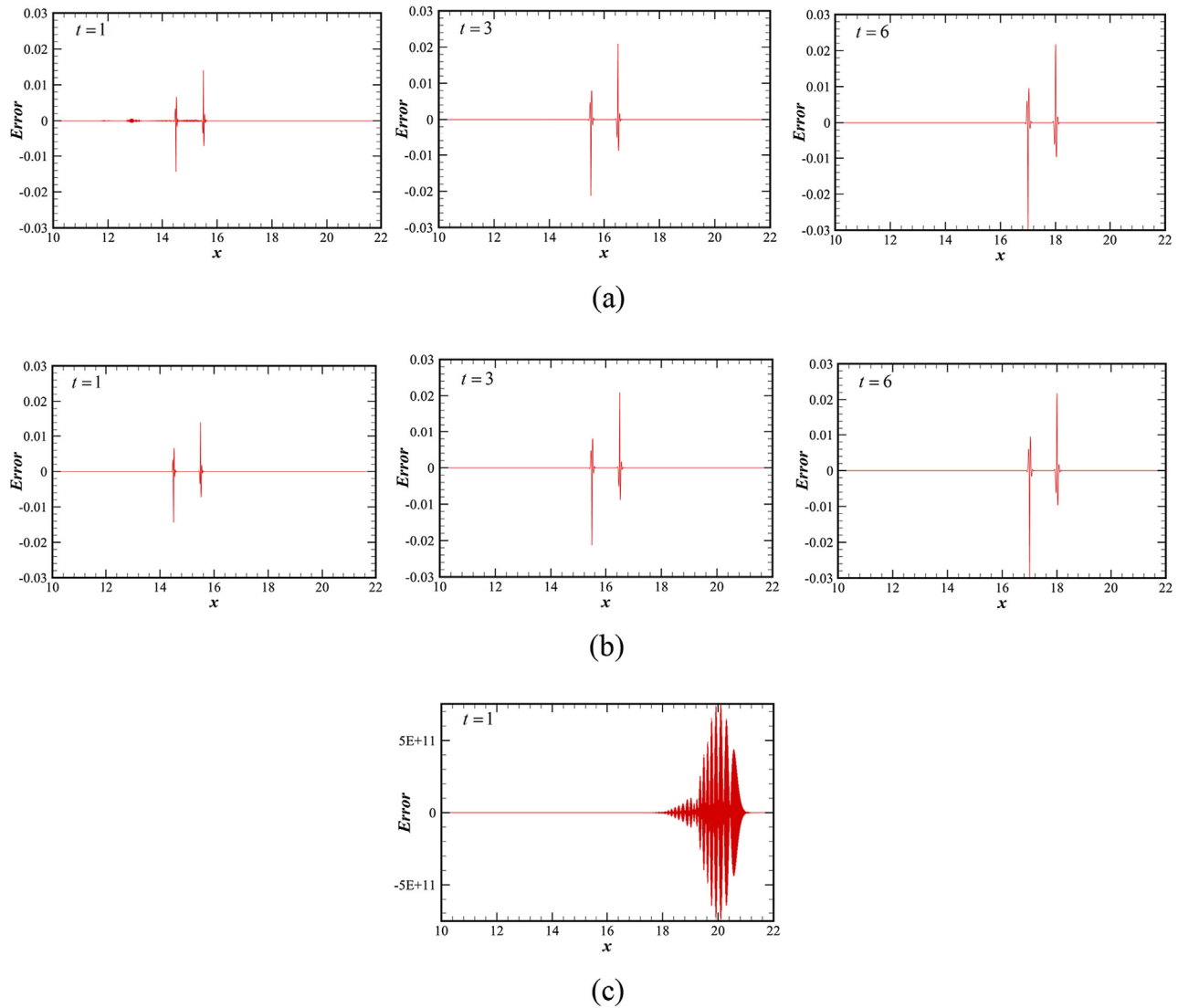


FIG. 13. The errors of three CCUSs for $Cr=0.768$: (a) CCS, (b) CCUS_DDB, and (c) CCUS_DRP.

$$\begin{cases} \frac{\partial u_i}{\partial x_i} = 0 \\ \frac{\partial u_i}{\partial t} + u_j \frac{\partial u_i}{\partial x_j} = -\frac{\partial p}{\partial x_i} + \frac{1}{Re} \frac{\partial^2 u_i}{\partial x_j^2}, \end{cases} \quad (35)$$

where u is the velocity, p is the pressure, and Re is the Reynolds number.

The two cases are all with periodic boundary conditions. The projection method⁴³ is adopted to solve the N-S equation. For spatial discretization, diffusion and convection terms are discretized by the sixth-order compact central scheme and the different compact upwind schemes, respectively. For temporal discretization, the third-order Runge–Kutta scheme is employed. The algebraic equations are solved by the algebraic multigrid method. The initial conditions, Re , and

mesh information will be introduced in the discussion of corresponding cases.

B. Taylor Green vortex

Taylor Green vortex is a benchmark case for unsteady incompressible flow, and it is usually used to evaluate the reliability of a program and the accuracy of a scheme.^{20,44} The computational domain in the present study is a unit square ($0 \leq x, y \leq 1$). For the governing equation [Eq. (35)], the initial condition is given as follows:

$$\begin{aligned} u(x, y, 0) &= -\cos(2\pi x)\sin(2\pi y), \\ v(x, y, 0) &= \sin(2\pi x)\cos(2\pi y), \\ p(x, y, 0) &= -\frac{1}{4} [\cos(4\pi x) + \cos(4\pi y)] \end{aligned} \quad (36)$$

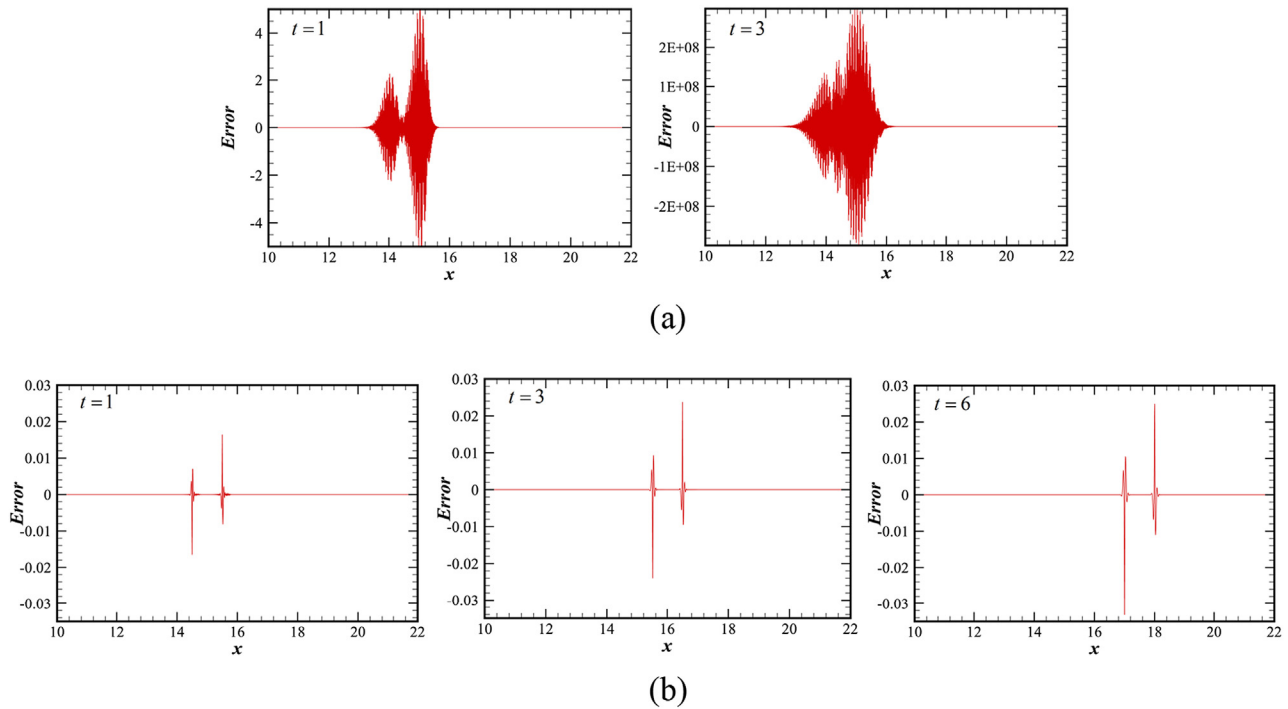


FIG. 14. The errors of two CCUSs for $Cr=0.975$: (a) CCS and (b) CCUS_DDB.

and the Reynolds number is given as 1000. The analytical solution can be obtained by using periodic boundary conditions in both directions and is shown by the following equation:

$$\begin{aligned}
 u(x, y, t) &= -\cos(2\pi x)\sin(2\pi y)e^{-\frac{8\pi^2}{Re}t}, \\
 v(x, y, t) &= \sin(2\pi x)\cos(2\pi y)e^{-\frac{8\pi^2}{Re}t}, \\
 p(x, y, t) &= -\frac{1}{4}[\cos(4\pi x) + \cos(4\pi y)]e^{-\frac{16\pi^2}{Re}t}.
 \end{aligned}
 \tag{37}$$

In the present study, five different sizes of grids (8×8 , 16×16 , 32×32 , 64×64 , and 128×128) are used. On the grid of 32×32 , all nine schemes can approximate the analytical solution quite well. To save space, only the results obtained by CCS on the grid of 32×32 are presented below.

Figure 15 is the contour map of u -velocity at different times. The amplitude of u -velocity at the initial time is the largest, and it decays with time due to the viscous dissipation, but the relative spatial distribution remains unchanged. These properties are consistent with the analytical solution. The u and v velocity components at different times are illustrated in Fig. 16, in which the predicted velocities agree well with the exact solution. To evaluate the error of all schemes quantitatively and calculate the convergence rate, the 2-Norm error defined as Eq. (38) is adopted to measure the average deviation, and the ∞ -Norm error defined as Eq. (39) is adopted to measure the maximum deviation,

$$L_2 = \|u - u_{exact}\|_2 = \sqrt{\frac{1}{N} \sum_{i=1}^N (u_i - u_{exact})^2}, \tag{38}$$

$$L_\infty = \|u - u_{exact}\|_\infty = \max_{1 \leq i \leq N} |u_i - u_{exact}|, \tag{39}$$

where N represents the total element number.

The numerical error with different mesh sizes (8×8 , 16×16 , 32×32 , 64×64 , and 128×128) obtained by nine compact schemes

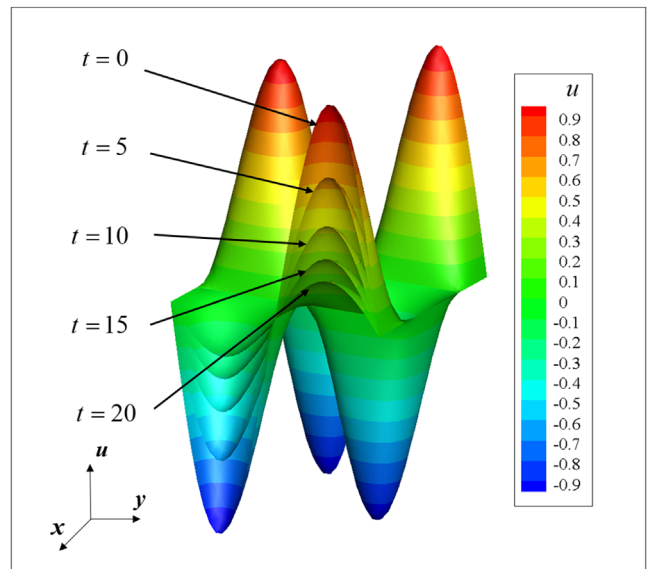


FIG. 15. Contour map of the u -velocity at different times.

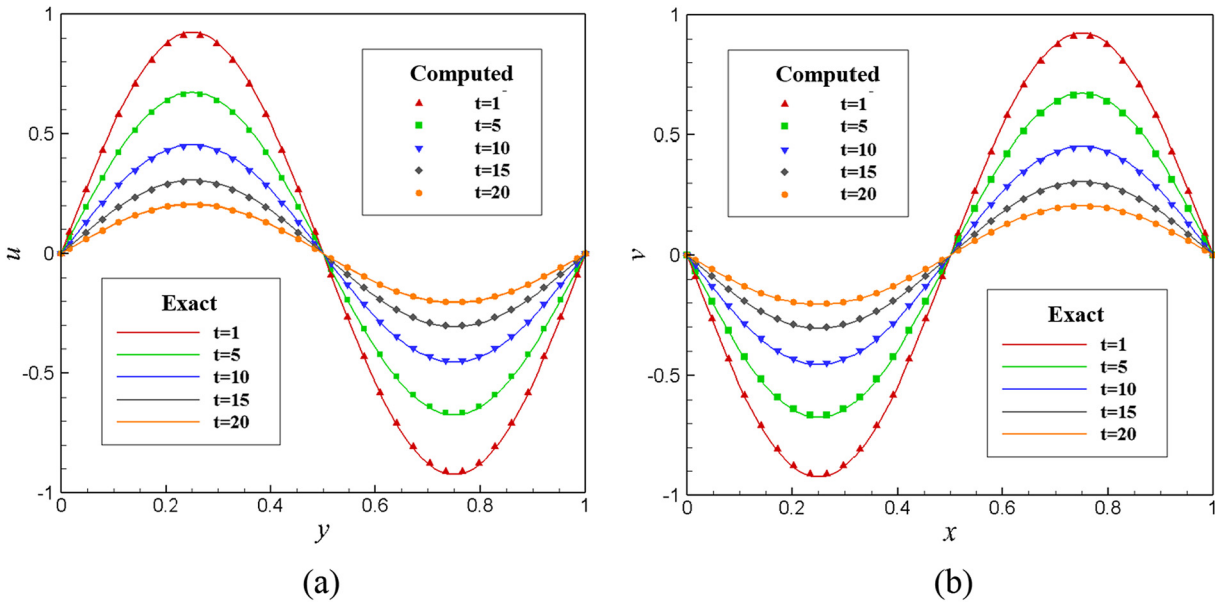


FIG. 16. Velocity distribution at different time: (a) u velocity vs y at $x = 0.5$ and (b) v -velocity vs x at $y = 0.5$.

are evaluated by 2-Norm error and ∞ -Norm error, and the corresponding results are illustrated in Fig. 17. The results for both errors show the same variation trend, and the difference between the maximum and average error is slight. In these double logarithmic figures, all the errors decrease linearly with a reduction in mesh size. The slopes of the lines represent the convergence rate. Among all the schemes compared, only the CCS is of the sixth-order accuracy, and its error is also the smallest. Other schemes are all of the fifth-order accuracy, among which the OCCUS_DDB has the minimum error. These schemes are sorted in the descending order of error as

$$\begin{aligned} & \text{OCCUS_DDB} < \text{OFCUS_DDB} < \text{SFCUS} < \text{OFCUS_DRP} \\ & < \text{OCCUS_DRP} < \text{ODCUS_DDB} < \text{SDCUS} < \text{ODCUS_DRP}. \end{aligned} \quad (40)$$

From the order list shown above, it is found that when the same optimization methods are applied, the errors of FCUS are always smaller than that of DCUS. It reveals again that the compact scheme with the function-biased stencil is superior to that with the derivative-biased stencil. On the other hand, when optimizing the schemes, no matter what stencil adopts, the scheme optimized by the DDB method, which

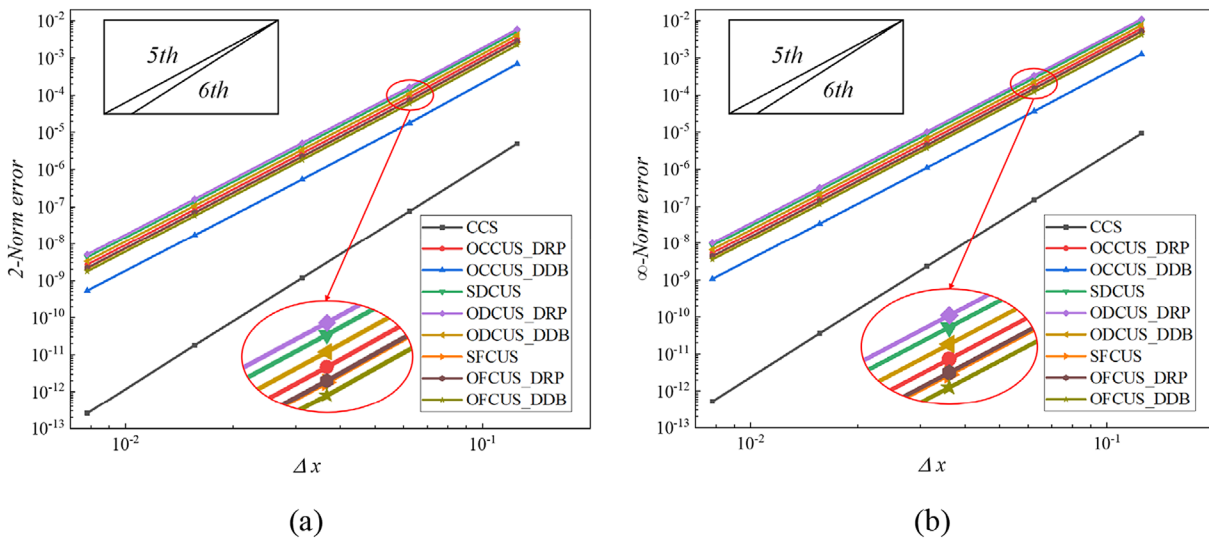


FIG. 17. Errors of different schemes: (a) 2-Norm error and (b) ∞ -Norm error.

considers both dissipation error and dispersion error, has smaller errors than that by the DRP method.

C. Double shear layers flow

The second case is the double shear layers flow that was proposed by Bell and Colella⁴⁵ and analyzed in detail by Brown *et al.*^{46,47} It is a classical case for testing the accuracy and resolution of a scheme, and many other researchers used this problem to evaluate their proposed schemes.^{17,20,32,48} The initial condition of the double shear layers flow is

$$\begin{aligned}
 u(x, y, t) &= \begin{cases} \tanh[\rho(y - 0.25)] & 0 \leq y \leq 0.5, \\ \tanh[\rho(0.75 - y)] & 0.5 < y \leq 1 \end{cases} \\
 v(x, y, t) &= \delta \sin(2\pi x),
 \end{aligned} \tag{41}$$

where the parameter ρ decides the initial thickness of the shear layer (the larger the ρ value, the thinner the shear layer), and δ is the amplitude of the initial disturbance. In this study, we chose $\delta = 0.05$, $\rho = 100$, and the Reynolds number $Re = 18\,000$.

The initial condition is drawn in Fig. 18. The direction of initial mainstream velocity u [Fig. 18(a)] changes twice, which results in large velocity gradients and forms two shear layers shown in Fig. 18(c). When the sinusoidal disturbance [Fig. 18(b)] is imposed on the y direction, the shear layer will be distorted, forming two large vortices in the layer. With the rolling up of the large vortices, the shear layer between the two vortices will become increasingly thinner, which causes larger difficulties for difference schemes to resolve the thin layer.

The numerical simulation results of double shear layers flow with nine different schemes are illustrated and compared. The double shear layers flow is different from the Taylor Green vortex case in that it is impossible to give an analytical solution of the governing equation with the initial condition like Eq. (41). Therefore, the simulations are conducted on the grids of 200×200 , 400×400 , and 800×800 , respectively. On the grid of 400×400 , the results with all these schemes are very close, and they are almost exactly the same based on the grid of 800×800 . It is reasonable to regard the result on the grid of 800×800 as the reference solution.

Figures 19 and 20 illustrate the results obtained by three central stencil compact upwind schemes at $t = 0.8$ and $t = 1.3$, respectively. As shown in Fig. 19, the shear layer has been distorted by the perturbation, forming large vortices at $t = 0.8$. Compared with the reference solution, there are some nonphysical oscillations, which are marked with red boxes in Fig. 19(a), near the large vortices when CCS is applied on the grid of 200×200 . However, these oscillations do not appear in the results with the two optimized schemes. As for OCCUS_DRP, the thin shear layer between the two vortices seems to be distorted, and there shows a tendency of forming a small vortex at the position marked with the blue circle, which is not observed for the cases with CCS and OCCUS_DDB. According to the reference solution, it can be known that the vortex is not supposed to exist. It is a kind of nonphysical or spurious vortex. At $t = 1.3$ (Fig. 20), the shear layer keeps rolling up. With the growing up of the main vortices, the shear layer is dragged thinner. The potential spurious vortex wrongly computed by OCCUS_DRP finally forms in Fig. 20(b). However, for OCCUS_DDB, Figs. 19(c) and 20(c) show that the results obtained by this scheme on the grid of 200×200 are the closest to the reference solution. Neither the oscillation nor the spurious vortex appears.

The oscillations shown in Fig. 19(a) arise from the wrong dispersion relation, and these oscillations are dissipated by two optimized upwind schemes [see Figs. 19(b) and 19(c)]. Nevertheless, the spurious vortex between the two large vortices appears and grows only in the simulation with OCCUS_DRP, indicating its formation mechanism differs from the oscillations in Fig. 19(a). Considering that the simulation results with CCS and OCCUS_DDB, which have a larger resolution for the dissipation relation, do not suffer from this problem, it is reasonable to assume that the spurious vortex at the center of the shear layer resulted from dissipation error. To verify this idea, the same problem of double shear layers flow is simulated by the spatial-explicit fourth-order central scheme (fourth-CS) and the third-order upwind-biased scheme (third-US).⁴⁹ The difference expressions and the modified wavenumbers of these two schemes are listed in Eqs. (42)–(45). From the modified wavenumbers, we can see that these two schemes have the same dispersion error and different dissipation errors,

Third-US:

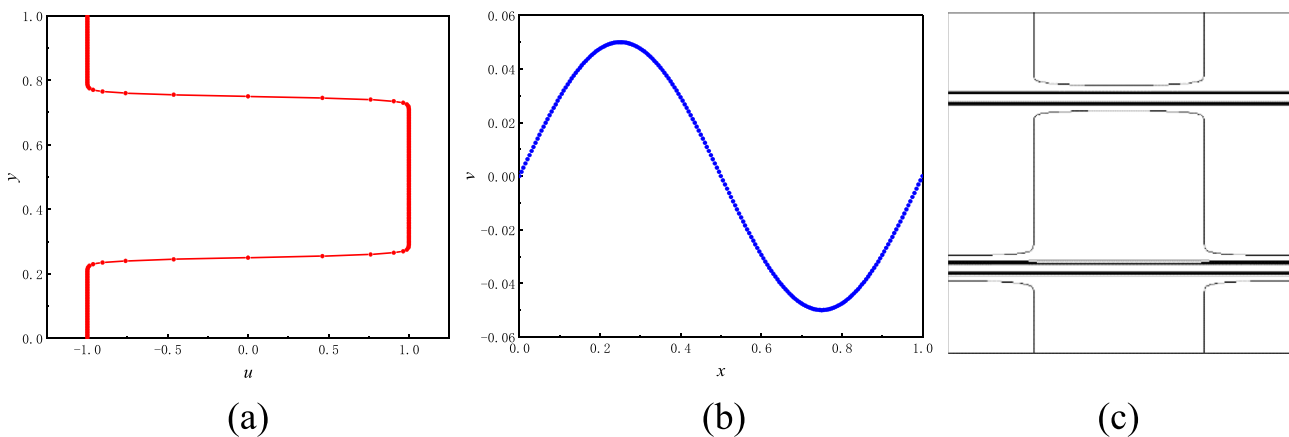


FIG. 18. The initial state of double shear layers flow: (a) u -velocity along the y direction, (b) v -velocity along the x direction, and (c) vorticity contour.

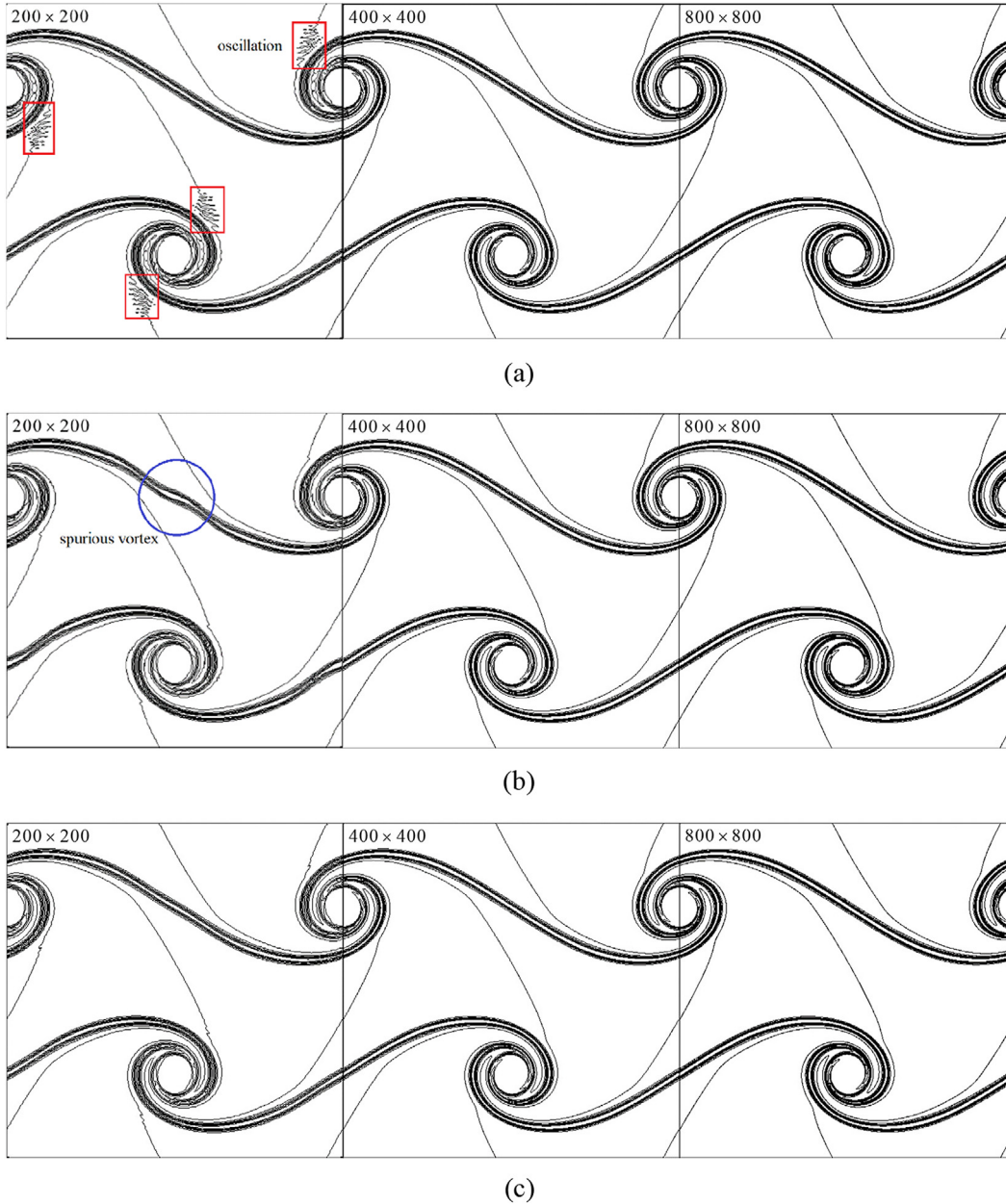


FIG. 19. Vorticity contours at $t = 0.8$ for (a) CCS, (b) OCCUS_DRP, and (c) OCCUS_DDB.

$$f'_i = \frac{2f_{i+1} + 3f_i - 6f_{i-1} + f_{i-2}}{6h}, \quad (42)$$

$$k_i h = \frac{1}{6}(8 \sin \alpha - \sin 2\alpha), \quad k_r h = -\frac{1}{6}(3 - 4 \cos \alpha + \cos 2\alpha). \quad (43)$$

Fourth-CS:

$$f'_i = \frac{8(f_{i+1} - f_{i-1}) - (f_{i+2} - f_{i-2})}{12h}, \quad (44)$$

$$k_r h = \frac{1}{6}(8 \sin \alpha - \sin 2\alpha), \quad k_i h = 0. \quad (45)$$

The vorticity contours of the double shear layers flow computed with fourth-CS and third-US are shown in Fig. 21. Similar to the results obtained by CCS, nonphysical oscillations exist in the results with fourth-CS because of the lack of dissipation. The shear layer between two large vortices remains straight without spurious vortices in Fig. 21(a). Figure 21(b) shows the results with third-US. As a kind of upwind

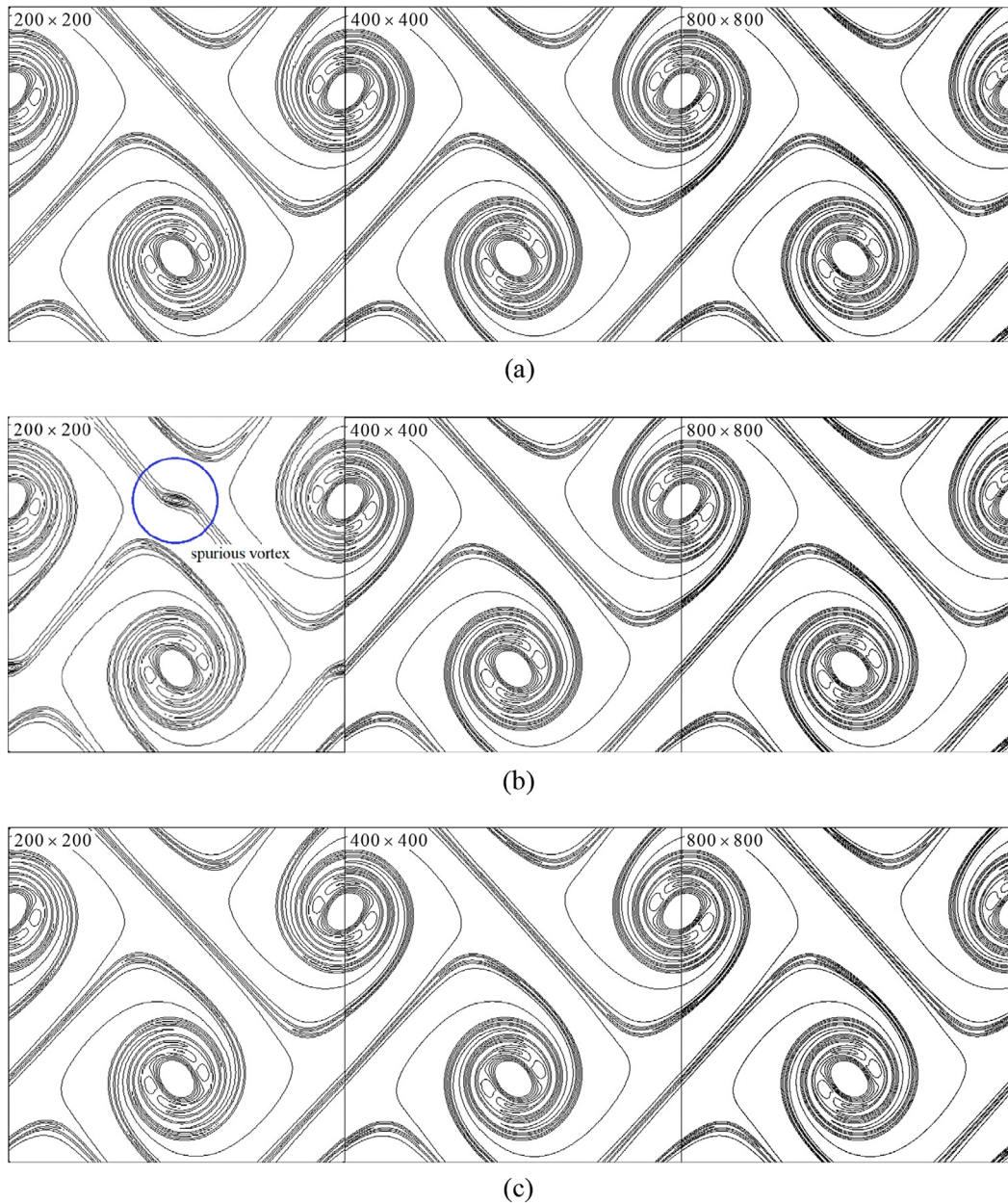
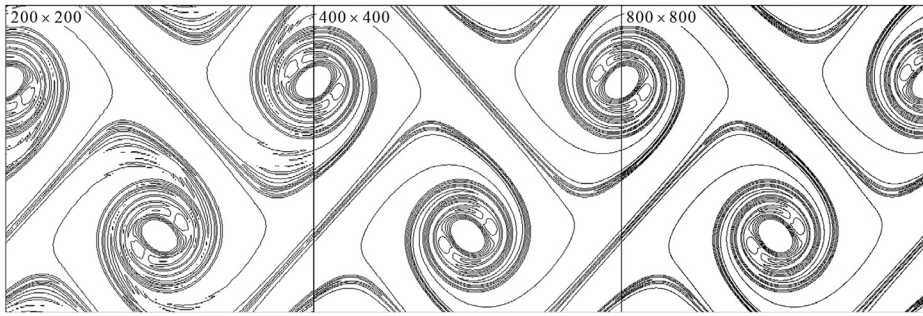


FIG. 20. Vorticity contours at $t = 1.3$ for (a) CCS, (b) OCCUS_DRP, and (c) OCCUS_DDB.

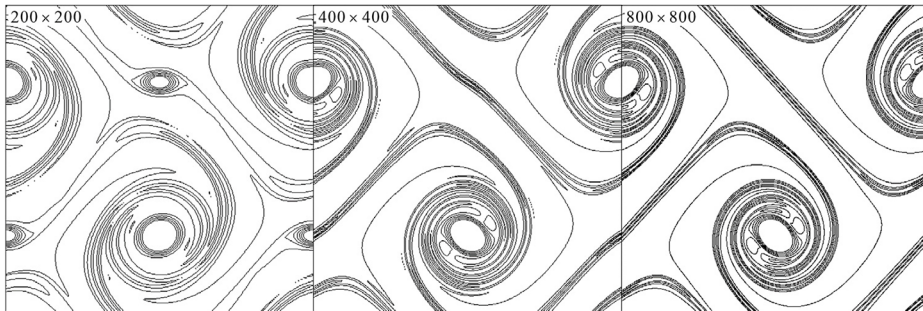
scheme, the inherent dissipation of third-US effectively eliminated the nonphysical oscillation, but at the same time, a large spurious vortex appears at the central location between the two main vortices. To further verify the above understanding, another pair of schemes, which are the first-order upwind scheme (first-US) and the second-order central scheme (second-CS), are compared for this problem. The same conclusions are obtained. For the sake of simplicity, it is not detailed. It can be concluded that the spurious vortices are

caused by the dissipation error, which provides theoretical support for the DDB optimization method.

Furthermore, the simulation results of the double shear layers flow based on SFCUS, SDCUS, as well as their optimized schemes, are illustrated in Figs. 22–24. These six schemes are all of fifth-order accuracy; their order and the resolution for dispersion relation are all higher than those of fourth-CS and second-US. However, the spurious vortices only appear in the cases with these fifth-order schemes rather

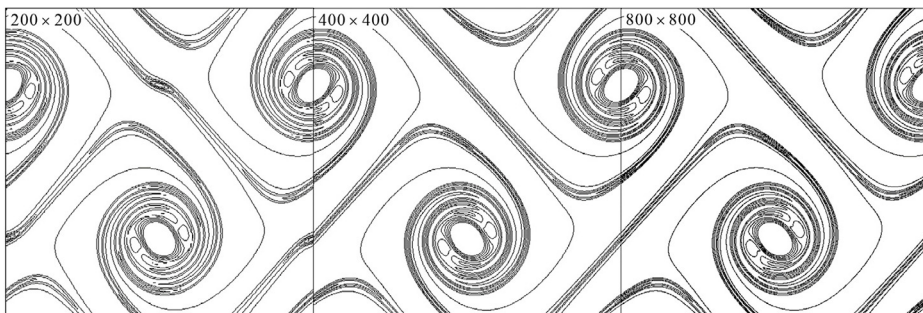


(a)

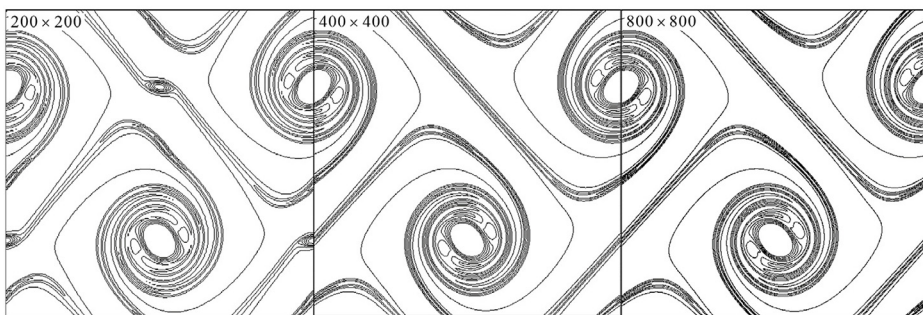


(b)

FIG. 21. Vorticity contours at $t = 1.3$ for (a) fourth-CS and (b) third-US.

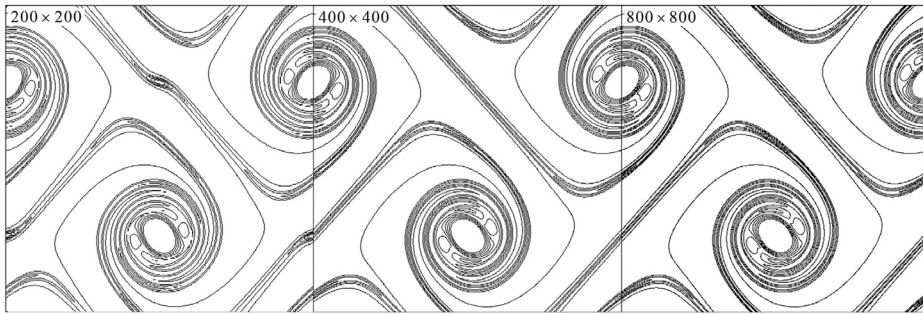


(a)

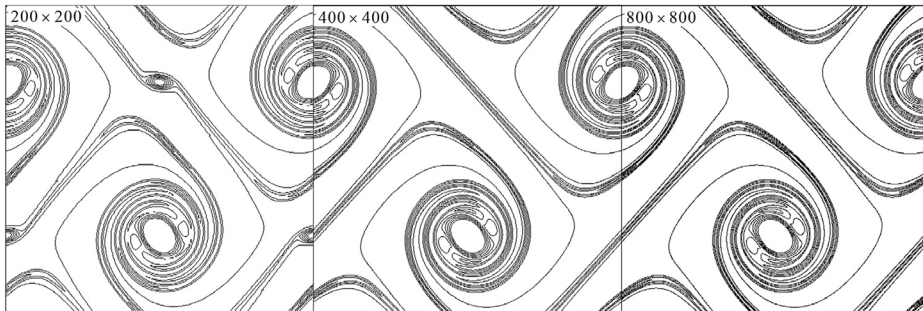


(b)

FIG. 22. Vorticity contours at $t = 1.3$ for (a) SFCUS and (b) SDCUS.

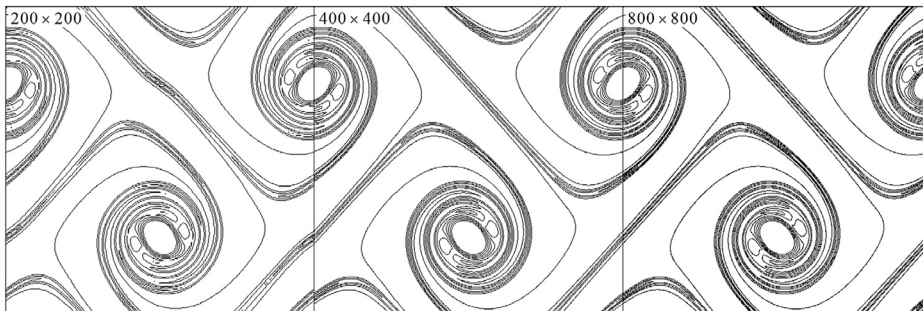


(a)

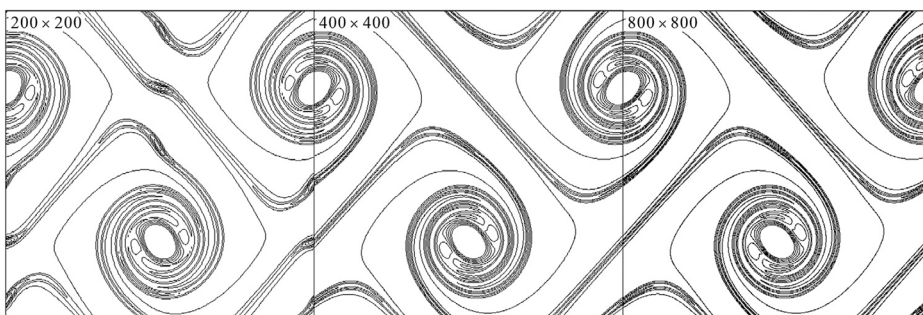


(b)

FIG. 23. Vorticity contours at $t = 1.3$ for (a) OFCUS_DRP and (b) ODCUS_DRP.



(a)



(b)

FIG. 24. Vorticity contours at $t = 1.3$ for (a) OFCUS_DDB and (b) ODCUS_DDB.

than fourth-CS or second-US. It reveals again that the cause of spurious vortices is related to dissipation error. By comparing Figs. 23(a) and 23(b) and comparing Figs. 24(a) and 24(b), we can see that no matter which optimization method is adopted, the spurious vortices obtained by the schemes with function-biased stencils are smaller than those with derivative-biased stencils, which is because the dissipation error of the FCUS is smaller than that of DCUS. On the other hand, compared with the results obtained by the standard schemes (Fig. 22), the spurious vortices calculated by DRP-optimized schemes (Fig. 23) even grow up a little. On the contrary, the schemes with DDB optimization (Fig. 24), which increases the resolution for dissipation relation, can suppress the formation of spurious vortices and capture the thin layer better.

V. CONCLUSIONS

In this paper, the resolution characteristics of three types of compact upwind schemes are analyzed. Also, a dispersion-dissipation-balancing optimization method is proposed to optimize these schemes. The main conclusions are drawn as follows:

1. The Fourier analysis shows that the standard form of FCUS has a wider wavenumber range of low dissipation error and low dispersion error than DCUS. The spatiotemporal spectral analysis proves that this conclusion is still valid for the optimized schemes and for time-space independent problem.
2. In the proposed optimization procedure of the DDB method, the dissipation error and dispersion error are considered simultaneously and kept in a proper balance. The spectral analysis indicates that the DDB optimization method is more suitable for the CCUS and FCUS, and the advantages of the DDB method are proved by the solution of the propagation of a ramp signal governed by the 1D wave equation.
3. The schemes optimized by the DDB method are superior to those optimized by the DRP method, in which the dissipation error is hardly considered. For the Taylor Green vortex case, the schemes optimized by the DDB method have smaller average errors and maximum errors than the DRP-optimized scheme. For the double shear layers flow case, the DDB-optimized schemes have enough dissipation to eliminate the nonphysical oscillation. They can effectively reduce and even totally suppress the formation of the spurious vortex, while the DRP-optimized scheme cannot.

ACKNOWLEDGMENTS

This work is supported by the Key Project of NNSFC (No. 51836005), the Foundation for Innovative Research Groups of the National Natural Science Foundation of China (No. 51721004), and the 111 Project (No. B16038).

AUTHOR DECLARATIONS

Conflict of Interest

The authors have no conflicts to disclose.

Author Contributions

Hao Ding: Conceptualization (equal); Formal analysis (equal); Investigation (equal); Methodology (equal); Writing – original draft

(equal). **Yujie Chen:** Investigation (equal); Methodology (equal); Writing – review & editing (equal). **Wenquan Tao:** Funding acquisition (equal); Methodology (equal); Supervision (equal); Writing – review & editing (equal).

DATA AVAILABILITY

The data that support the findings of this study are available from the corresponding author upon reasonable request.

REFERENCES

- ¹S. K. Lele, "Compact finite difference schemes with spectral-like resolution," *J. Comput. Phys.* **103**, 16–42 (1992).
- ²T. K. Sengupta, G. Ganerwal, and S. De, "Analysis of central and upwind compact schemes," *J. Comput. Phys.* **192**, 677–694 (2003).
- ³T. K. Sengupta, *High Accuracy Computing Methods: Fluid Flows and Wave Phenomena* (Cambridge University Press, Cambridge, MA, 2013).
- ⁴T. K. Sengupta, S. K. Sircar, and A. Dipankar, "High accuracy schemes for DNS and acoustics," *J. Sci. Comput.* **26**, 151–193 (2006).
- ⁵S. Nagarajan, S. K. Lele, and J. H. Ferziger, "A robust high-order compact method for large eddy simulation," *J. Comput. Phys.* **191**, 392–419 (2003).
- ⁶J. Suh, S. H. Frankel, L. Mongeau, and M. W. Plesniak, "Compressible large eddy simulations of wall-bounded turbulent flows using a semi-implicit numerical scheme for low Mach number aeroacoustics," *J. Comput. Phys.* **215**, 526–551 (2006).
- ⁷S. Laizet and E. Lamballais, "High-order compact schemes for incompressible flows: A simple and efficient method with quasi-spectral accuracy," *J. Comput. Phys.* **228**, 5989–6015 (2009).
- ⁸F. Bauer, S. Tardu, and O. Doche, "Efficiency of high accuracy DRP schemes in direct numerical simulations of incompressible turbulent flows," *Comput. Fluids* **107**, 123–140 (2015).
- ⁹S. Bhole and T. K. Sengupta, "Roles of bulk viscosity on transonic shock-wave/boundary layer interaction," *Phys. Fluids* **31**, 096101 (2019).
- ¹⁰T. Luo, J. Wang, C. Xie, M. Wan, and S. Chen, "Effects of compressibility and Atwood number on the single-mode Rayleigh-Taylor instability," *Phys. Fluids* **32**, 012110 (2020).
- ¹¹J. P. Boyd, *Chebyshev and Fourier Spectral Methods*, 2nd ed. (revised) (Dover Publications, Inc., New York, 2001).
- ¹²N. A. Adams and K. Shariff, "A high-resolution hybrid compact-ENO scheme for shock-turbulence interaction problems," *J. Comput. Phys.* **127**, 27–51 (1996).
- ¹³X. Zhong, "High-order finite-difference schemes for numerical simulation of hypersonic boundary-layer transition," *J. Comput. Phys.* **144**, 662–709 (1998).
- ¹⁴D. Fu and Y. Ma, "Upwind compact schemes and applications," in *Proceedings of the 5th International Symposium on Computational Fluid Dynamics* (Japan Society of Computational Fluid Dynamics, 1993), pp. 184–190.
- ¹⁵Q. Qin, Z. A. Xia, and Z. F. Tian, "High accuracy numerical investigation of double-diffusive convection in a rectangular enclosure with horizontal temperature and concentration gradients," *Int. J. Heat Mass Transfer* **71**, 405–423 (2014).
- ¹⁶D. Fu and Y. Ma, "A high order accurate difference scheme for complex flow fields," *J. Comput. Phys.* **134**, 1–15 (1997).
- ¹⁷Y. X. Sun and Z. F. Tian, "High-order upwind compact finite-difference lattice Boltzmann method for viscous incompressible flows," *Comput. Math. Appl.* **80**, 1858–1872 (2020).
- ¹⁸J. Chen, P. Yu, H. Ouyang, and Z. F. Tian, "A novel parallel computing strategy for compact difference schemes with consistent accuracy and dispersion," *J. Sci. Comput.* **86**, 5 (2021).
- ¹⁹Z. Tian, X. Liang, and P. Yu, "A higher order compact finite difference algorithm for solving the incompressible Navier–Stokes equations," *Int. J. Numer. Methods Eng.* **88**, 511–532 (2011).
- ²⁰A. Shah, L. Yuan, and A. Khan, "Upwind compact finite difference scheme for time-accurate solution of the incompressible Navier–Stokes equations," *Appl. Math. Comput.* **215**, 3201–3213 (2010).

- ²¹P. Fan, “The standard upwind compact difference schemes for incompressible flow simulations,” *J. Comput. Phys.* **322**, 74–112 (2016).
- ²²N. Gui, L. Ge, P. Cheng, X. Yang, J. Tu, and S. Jiang, “Comparative assessment and analysis of Rortex vortex in swirling jets,” *J. Hydrodyn.* **31**, 495–503 (2019).
- ²³M. K. Hasan and A. Gross, “Higher-order-accurate numerical method for temporal stability simulations of Rayleigh–Bénard–Poiseuille flows,” *Int. J. Numer. Methods Fluids* **93**, 127–147 (2021).
- ²⁴M. K. Hasan and A. Gross, “Numerical instability investigation of inward radial Rayleigh–Bénard–Poiseuille flow,” *Phys. Fluids* **33**, 034120 (2021).
- ²⁵Z. He, X. Li, D. Fu, and Y. Ma, “A 5th order monotonicity-preserving upwind compact difference scheme,” *Sci. China Phys., Mech. Astron.* **54**, 511–522 (2011).
- ²⁶Y. Li, “Wavenumber-extended high-order upwind-biased finite-difference schemes for convective scalar transport,” *J. Comput. Phys.* **133**, 235–255 (1997).
- ²⁷A. K. De and V. Eswaran, “Analysis of a new high resolution upwind compact scheme,” *J. Comput. Phys.* **218**, 398–416 (2006).
- ²⁸C. H. Yu, Y. G. Bhumkar, and T. W. H. Sheu, “Dispersion relation preserving combined compact difference schemes for flow problems,” *J. Sci. Comput.* **62**, 482–516 (2015).
- ²⁹C. K. W. Tam and J. C. Webb, “Dispersion-relation-preserving finite difference schemes for computational acoustics,” *J. Comput. Phys.* **107**, 262–281 (1993).
- ³⁰Y. G. Bhumkar, T. W. H. Sheu, and T. K. Sengupta, “A dispersion relation preserving optimized upwind compact difference scheme for high accuracy flow simulations,” *J. Comput. Phys.* **278**, 378–399 (2014).
- ³¹B. Zhao and Z. Tian, “High-resolution high-order upwind compact scheme-based numerical computation of natural convection flows in a square cavity,” *Int. J. Heat Mass Transfer* **98**, 313–328 (2016).
- ³²P. X. Yu and Z. F. Tian, “An upwind compact difference scheme for solving the stream function–velocity formulation of the unsteady incompressible Navier–Stokes equation,” *Comput. Math. Appl.* **75**, 3224–3243 (2018).
- ³³J. W. Kim and D. J. Lee, “Optimized compact finite difference schemes with maximum resolution,” *AIAA J.* **34**, 887–893 (1996).
- ³⁴M. Bikash, G. Naveen, and Y. G. Bhumkar, “Direct simulation of sound generation by a two-dimensional flow past a wedge,” *Phys. Fluids* **30**, 096101 (2018).
- ³⁵N. Ganta, B. Mahato, and Y. G. Bhumkar, “Modulation of sound waves for flow past a rotary oscillating cylinder in a non-synchronous region,” *Phys. Fluids* **31**, 096103 (2019).
- ³⁶N. Ganta, B. Mahato, and Y. G. Bhumkar, “Analysis of sound generation by flow past a circular cylinder performing rotary oscillations using direct simulation approach,” *Phys. Fluids* **31**, 026104 (2019).
- ³⁷B. Mahato, N. Ganta, and Y. G. Bhumkar, “Mitigation of aerodynamic sound for a laminar flow past a square cylinder using a pair of cowl plates,” *Phys. Fluids* **32**, 076108 (2020).
- ³⁸J. Q. Yang and B. X. Zhao, “Numerical investigation of double-diffusive convection in rectangular cavities with different aspect ratio I: High-accuracy numerical method,” *Comput. Math. Appl.* **94**, 155–169 (2021).
- ³⁹T. K. Sengupta and A. Dipankar, “A comparative study of time advancement methods for solving Navier–Stokes equations,” *J. Sci. Comput.* **21**, 225–250 (2004).
- ⁴⁰T. K. Sengupta, A. Dipankar, and P. Sagaut, “Error dynamics: Beyond von Neumann analysis,” *J. Comput. Phys.* **226**, 1211–1218 (2007).
- ⁴¹T. K. Sengupta, Y. G. Bhumkar, M. K. Rajpoot, V. K. Suman, and S. Saurabh, “Spurious waves in discrete computation of wave phenomena and flow problems,” *Appl. Math. Comput.* **218**, 9035–9065 (2012).
- ⁴²S. Gottlieb and C. W. Shu, “Total variation diminishing Runge–Kutta schemes,” *Math. Comput.* **67**, 73–85 (1998).
- ⁴³D. L. Brown, R. Cortez, and M. L. Minion, “Accurate projection methods for the incompressible Navier–Stokes equations,” *J. Comput. Phys.* **168**, 464–499 (2001).
- ⁴⁴A. Shah, L. Yuan, and S. Islam, “Numerical solution of unsteady Navier–Stokes equations on curvilinear meshes,” *Comput. Math. Appl.* **63**, 1548–1556 (2012).
- ⁴⁵J. B. Bell and P. Colella, “A second-order projection method for the incompressible Navier–Stokes equations,” *J. Comput. Phys.* **85**, 257–283 (1989).
- ⁴⁶D. L. Brown, “Performance of under-resolved two-dimensional incompressible flow simulations,” *J. Comput. Phys.* **122**, 165–183 (1995).
- ⁴⁷M. L. Minion and D. L. Brown, “Performance of under-resolved two-dimensional incompressible flow simulations—II,” *J. Comput. Phys.* **138**, 734–765 (1997).
- ⁴⁸O. G. Nwogu, “A flexion-based approach for the simulation of turbulent flows,” *Phys. Fluids* **32**, 055101 (2020).
- ⁴⁹M. A. N. Rai and P. Moin, “Direct simulations of turbulent flow using finite-difference schemes,” in 27th Aerospace Sciences Meeting (1989).